

COMPARISON OF CRUSTAL MAGMATIC STORAGE AT ALEUTIAN
VOLCANOES, GARELOI AND KANAGA, USING TELESEISMIC
RECEIVER FUNCTION ANALYSIS

A THESIS SUBMITTED TO THE UNDERGRADUATE DIVISION OF
THE UNIVERSITY OF HAWAI'I AT MĀNOA IN PARTIAL
FULFILLMENT OF THE REQUIREMENTS
FOR THE DEGREE OF

BACHELOR OF SCIENCE
IN
EARTH SCIENCES — RESEARCH EMPHASIS TRACK

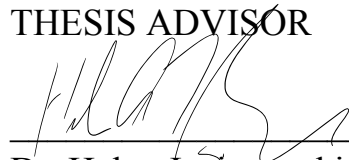
May 2024

By
Casey Wandasan

Thesis Advisor:
Dr. Helen Janiszewski

I certify that I have read this thesis and that, in my opinion, it is satisfactory in scope and quality.

THESIS ADVISOR

A handwritten signature in black ink, appearing to read 'H. Janiszewski', written over a horizontal line.

Dr. Helen Janiszewski, Department of Earth Sciences

Copyright 2024
by
Casey Wandasan

Acknowledgements

This work is funded through the National Science Foundation Award Number EAR 2052829 and is made possible via data obtained from stations maintained by the Alaska Volcano Observatory.

I would like to thank Dr. Helen Janiszewski for providing me with the opportunity to do undergraduate research, attend conferences, and advise me on career development. Dr. Janiszewski's guidance and assistance shaped my career path by challenging me in both research and professional growth. I would not be where I am today without her.

I would also like to thank Dr. Janiszewski's research group of graduate students who helped me along the way in both research and in career advancement. I am personally grateful to the graduate student Ian Wynn for helping me with programming issues and in general, the guidance he provided.

I am also appreciative to the AVO staff, particularly Dr. John A. Power and Dr. Matthew Haney, who aided our research project by providing sources and added new insight into the Aleutian volcanoes we are studying.

Lastly, I'd like to thank my family and friends for their continuous support and encouragement such as traveling to the Continental U.S. for the first time and applying to schools elsewhere from Hawai'i.

Abstract

The Aleutian arc is of considerable interest for geophysical and geologic investigations due to an abundance of 53 historically active volcanoes with several eruptions per year. Characterization of crustal magma storage depths and establishing ties to laterally variable subduction processes along the arc have been challenging due to the remote and harsh environment. In 2019, the Alaska Volcano Observatory conducted upgrades to the seismic network on Gareloi and Kanaga volcanoes in the Andreanof Islands. These upgrades increased the number of three-component broadband seismometers at these volcanoes to five and six, respectively. While these volcanoes are located only ~100 km from each other, there are key differences in observed seismic activity. While both have seismicity persistent through the upper- to mid-crust, Gareloi's rate of low-frequency seismicity is higher, and it is relatively devoid of volcano-tectonic earthquakes. To better understand what this might imply for crustal magma storage, we use the receiver function (RF) technique to provide independent constraints on subsurface magmatic system geometry.

We calculate RFs from teleseismic earthquakes with $>M5.5$ from 2019 to 2023. We use the P-to-S converted phases to constrain depths and velocities of abrupt boundaries in the crust related to magmatic structure. Both Gareloi and Kanaga provide good targets for this technique; each station produced on average ~419 RFs with overlapping ray path coverage between stations. We observe arrivals consistent with features in the mid-to-deep crust (~12–25 km depth) at both volcanoes. In addition, the RFs display complex patterns of back azimuthal variability that vary across stations at an individual volcano. We aim to

interpret these complex arrivals and compare magma storage at the two volcanoes through forward modeling constraining crustal velocities.

Table of Contents

Acknowledgements	iv
Abstract	v
Table of Contents	vii
List of Tables	viii
List of Figures	ix
List of Abbreviations	xi
Chapter 1: Introduction	1
Chapter 2: Methods	5
2.1 Instruments and Data.....	5
2.2 Receiver Function Analysis.....	8
Chapter 3: Results	12
3.1 Directional Variability.....	12
3.2 Synthetic Modeling	19
Chapter 4: Discussion	26
Chapter 5: Conclusion	28
Appendix A: Cross-Correlation Plots	30
Appendix B: 2-layer RMSD Plots	33
References	41

List of Tables

Table 1: Station Metadata

Table 2: Number of RFs Used in this Study

List of Figures

Figure 1: Map of the Aleutian arc with yellow arrow labels showing the subduction direction of the Pacific plate beneath the North American plate. The two volcanoes of interest, Gareloi and Kanaga, are located near the center of the arc.

Figure 2: (A) All five stations on the island volcano Gareloi. (B) All six stations on the island of Kanaga. Notice that station KIMD is the most southern station, located ~18 km from the volcano edifice.

Figure 3: Earthquake event map of teleseismic events 20–100° used for RF analysis. (A) Gareloi used 776 unique earthquake events to produce 5312 RFs across the five stations prior to quality control. (B) Kanaga used 711 unique earthquake events to produce 6789 RFs across the six stations prior to quality control.

Figure 4: An example station, KINC on the island of Kanaga. (A) A RF stack. (B) The ray path coverage plot for the same station. Both at $\text{SNR} \geq 4$.

Figure 5: Scatter plots of (A) Gareloi and (B) Kanaga of the maximum and minimum amplitudes of depth migrated 15° binned RFs (at all stations at a volcano) versus depth and organized by direction towards the volcano, with 0° facing towards the volcano and -180° and 180° facing away from the volcano, with angles increasing clockwise. Triangles are maximums, and circles are minimums. Blue represents positive polarity, and red represents negative polarity. Through visual assessment, dashed lines were drawn to highlight patterns of positive maximum and negative minimum at consistent depths: (A) Gareloi with -80° to 90° and (B) Kanaga with -80° to 80°.

Figure 6: RFs (depth migrated, 15° binned) from all stations (except AVKIMD or station KIMD at Kanaga), whose ray path points towards and away from the volcano edifice were plotted with their corresponding ray path coverage plots. Cutoff angles for toward and away were determined by Figure 5. (A) RFs pointing toward Gareloi and ray path coverage plot (E). (B) RFs pointing away from Gareloi and ray path coverage plot (F). (C) RFs pointing towards Kanaga and ray path coverage plot (G). (D) RFs pointing away from Kanaga and ray path coverage plot.

Figure 7: Cross-correlation plot between 15° RF bins with respect to the azimuthal separation or direction from the volcano edifice: 0° is pointing toward the volcano and -180° and 180° are pointing away from the volcano, with angles increasing clockwise. (A) AVGAEA is the station GAEA and is located east-southeast from the Gareloi's edifice. (B) AVKICM is the station KICM and is located west-southwest of the volcano Kanaga. (C) AVKIMD is the station KIMD, which is located south-southwest of the volcano Kanaga and is the farthest station from the volcano on Kanaga Island. See Appendix B for the cross-correlation plots at all stations for both volcanoes.

Figure 8: Synthetic RFs plotted against a 15° back azimuthal binned RF pointing towards the volcano edifice and away for both a 2-layer model and a 4-layer model. The corresponding velocity models are plotted. The RMSD between the synthetic and binned RFs is listed, and the number of individual RFs in each bin is listed. (A) Gareloi example stations: GANE (towards) and GASW (away). (B) Kanaga example stations: KINC (towards) and KIMD (away).

Figure 9: RMSD plots computed from 15° back azimuthal binned RFs and synthetic RFs for both a 2-layer and 4-layer velocity model at Gareloi and Kanaga. Shown here are only the models with the lowest RMSD at all stations for the 2-layer and 4-layer model at each volcano. (A) Gareloi 2-layer velocity model. (B) Gareloi 4-layer velocity model. (C) Kanaga 2-layer velocity model. (D) Kanaga 4-layer velocity model.

Figure 10: RMSD difference plots for (A) Gareloi and (B) Kanaga. The RMSD difference is calculated by subtracting the 2-layer model RMSD from the 4-layer model RMSD. The models in Figure 9 were used to produce these two plots. Positive values (blue) imply a better fit to the 2-layer model. Negative values (yellow/red) imply a better fit to the 4-layer model.

List of Abbreviations

Abbreviations	Definition
AVO	Alaska Volcano Observatory
EarthScope DMC	EarthScope Data Management Center
BHE	Broadband High Gain East-West (Horizontal) Velocity Sensor/Seismometer
BHN	Broadband High Gain North-South (Horizontal) Velocity Sensor/Seismometer
BHZ	Broadband High Gain Vertical Velocity Sensor/Seismometer
BDF	Broadband D Infrasound Pressure Sensor
ZRT	Vertical-radial-transverse
RF / RFs	Receiver Function / Receiver Functions
RMSD	Root-Mean-Square Deviation

Chapter 1: Introduction

Processes along volcanic arcs result in variable magmatic structures within the overlying crust above the subducting slab. Often, multiple factors contribute to the abundance of or absence of geophysical indicators of magmatic storage and subsequent eruption frequency and pattern, with local seismicity being an indicator of such phenomena (Buurman et al., 2014). Examples that contribute to the variable magmatic crustal structure include parameters such as the age of the subducting slab, convergence rate, crustal stress regimes, crustal thickness, magma composition, and inclusion of water via fracture zones or through sediments (Buurman et al., 2014; Larsen, 2016). Furthermore, the pathways magma and gases traverse within the crust may be complicated by magma differentiation, magma degassing and crystallization, and alterations of viscosity and temperature, all of which impact the depths of crustal magmatic storage beneath arc volcanoes (Larsen, 2016). The nature of crustal magmatic storage along subduction zones is not fully understood; further research at specific volcanoes of interest along arcs is beneficial to understanding these relationships.

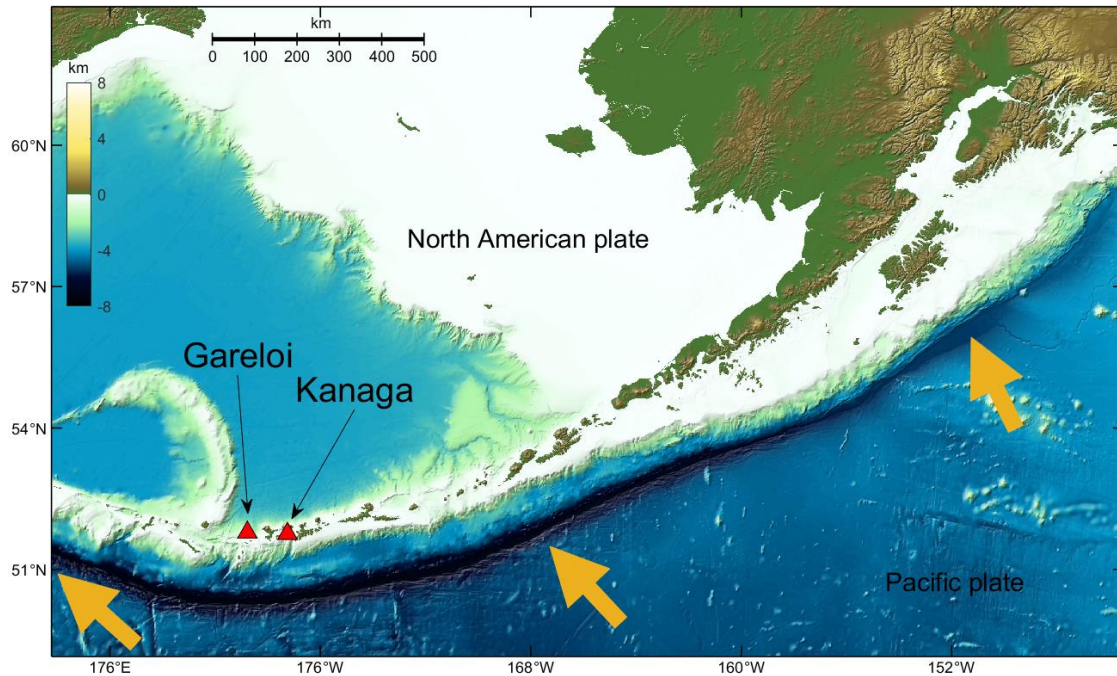


Figure 1: Map of the Aleutian arc with yellow arrow labels showing the subduction direction of the Pacific plate beneath the North American plate. The two volcanoes of interest, Gareloi and Kanaga, are located near the center of the arc.

The Alaska-Aleutian volcanic arc is an excellent location for along-arc geophysical and geologic investigations of crustal magmatic storage due to its 53 historically active volcanoes with several eruptions per year (Dixon et al., 2019). The arc extends for ~4000 km, spanning from Kamchatka Peninsula, Russia, in the west to mainland Alaska in the U.S. in the east. It is the result of the subduction of the Pacific Plate beneath the North American Plate (Buurman et al., 2014), with convergence rates ranging from 5.7 to 7.7 cm/yr (Figure 1). Subduction transitions from near-perpendicular to oblique from east to west, with the far western end nearly a right lateral strike-slip (DeMets et al., 2010). To the west of 172°W, the crust of the forearc can be divided into crustal blocks that rotate clockwise, leading to areas of local crustal compression and extension along-strike (Geist et al., 1988). The arc also subducts two fracture zones: the Aja Fracture Zone to the east

and the Amlia Fracture Zone near the center of the arc (Ryan et al., 2012; Maus et al., 2009). Both fracture zones are bathymetric highs that are thought to be associated with increased subducted sediment and/or mantle serpentinization, which contribute to increased magmatic flux (Buurman et al., 2014; Singer et al., 2007). Furthermore, there is along-arc variability in regional magma composition, from more felsic in the east to more mafic in the west (Buurman et al., 2014). This complexity along the Aleutian arc makes it an excellent candidate for further investigation of the impacts of subduction properties on crustal magma storage.

Here, we examine two active, proximal Aleutian volcanoes with distinctive eruptive histories, Gareloi and Kanaga, with the goal of better understanding their subsurface magma storage structure. Gareloi and Kanaga are located in the Andreanof Islands in the central Aleutians and are both excellent candidates for seismic imaging. Gareloi is a stratovolcano that has two summits reaching ~1570 m in elevation and overlooks a 4 km-long southeast-trending fissure consisting of 13 craters created by a 1929 eruption. In recorded history, there have been 12 confirmed eruptions, with the most recent eruption in 1989 (Miller et al., 1998). Three submarine avalanche debris located north, northwest, and east of the volcano are indicative of edifice collapse (Coombs et al., 2007). In comparison, Kanaga is a stratovolcano located on Kanaga Island. It is situated within the Kanaton caldera, which forms a 760 m high ridge on the southeast side of the volcano and a 30 km submarine avalanche debris on the north-northwest side of the caldera (Miller et al., 1998; Coombs et al., 2007). It has been determined that Kanaga underwent 18 confirmed Holocene eruptions, with the latest eruption in December 2023 (Global Volcanism Program, 2023). The two volcanoes have markedly different patterns of

seismicity beneath their edifices. Gareloi predominantly experiences low frequency earthquakes of magnitude 2–3, whereas Kanaga frequently experiences volcanic-tectonic earthquakes with magnitudes less than 1 (Buurman et al., 2014). Despite these intriguing variations, geophysical research into these remote and uninhabited volcanic islands is limited. Recent upgrades by the Alaska Volcano Observatory (AVO) in 2019 replaced 1-component short-period instruments with 3-component broadband seismometers. This enables us to use the seismic receiver function technique to constrain crustal magmatic structures beneath the two volcanoes for the first time. We use both real and synthetic receiver functions to create a simple velocity model beneath the volcanoes and compare them. This comparison will provide insight into regional subduction trends.

Chapter 2: Methods

2.1 Instruments and Data

We analyze seismic data from all broadband, three-component seismic stations installed at Gareloi and Kanaga volcanoes. At Gareloi, five stations are installed encircling the volcano summit, located within a 4.6 km radius (Figure 2). At Kanaga, there are six stations in total. Five are deployed central to the summit, within 7.9 km, but one station (KIMD) is located ~18.5 km south-southwest of the summit. All stations are part of the permanent AVO seismic network (network code, AV). These permanent instruments telemeter real-time data, which is archived at the EarthScope Data Management Center (DMC). See Table 1 for more information on each station.

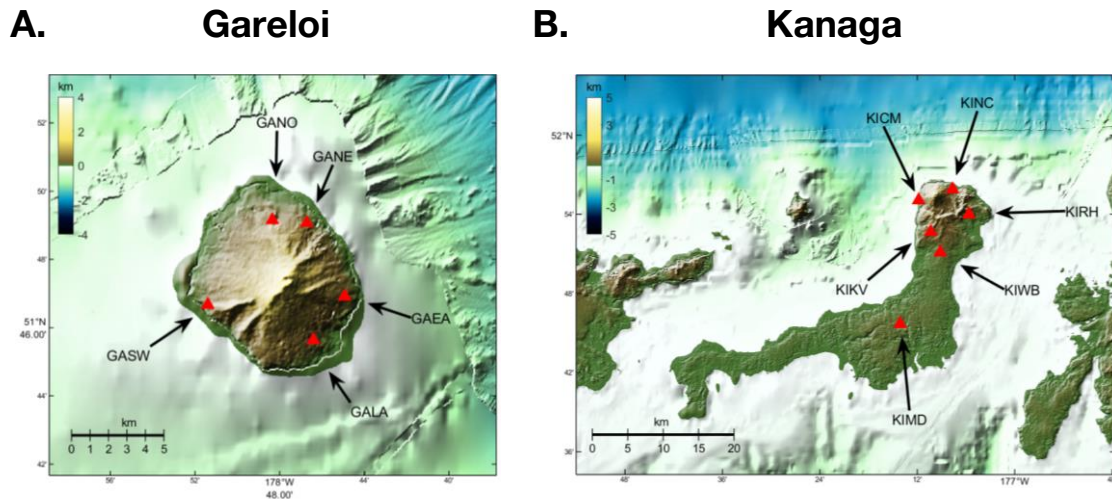


Figure 2: (A) All five stations on the island volcano Gareloi. (B) All six stations on the island of Kanaga. Notice that station KIMD is the most southern station, located ~18 km from the volcano edifice.

Table 1: Station Metadata

Station	Instrument/Channel	Latitude	Longitude	Station Elevation (m)	Distance to Edifice (km)
GAEA	Velocity Sensor (BHE, BHN, BHZ); Pressure (BDF) [50.0 Hz]	51.7819	-178.7488	326	3.2369
GALA	Velocity Sensor (BHE, BHN, BHZ); Pressure (BDF) [50.0 Hz]	51.760629	-178.77365	315	3.5534
GANE	Velocity Sensor* (BHE, BHN, BHZ); Pressure** (BDF) [50.0 Hz]	51.817787	-178.77859	325	3.2664
GANO	Velocity Sensor* (BHE, BHN, BHZ) [50.0 Hz]	51.8192	-178.80580	451	3.3467
GASW	Velocity Sensor* (BHE, BHN, BHZ); Pressure** (BDF) [50.0 Hz]	51.777633	-178.856549	248	4.5171
KICM	Velocity Sensor* (BHE, BHN, BHZ) [50.0 Hz]	51.91896	-177.19559	183	1.9447
KIKV	Velocity Sensor* (BHE, BHN, BHZ) [50.0 Hz]	51.878494	-177.17061	411	4.9521
KIMD	Velocity Sensor* (BHE, BHN, BHZ) [50.0 Hz]	51.761504	-177.235207	173.1	18.5416
KINC	Velocity Sensor* (BHE, BHN, BHZ); Pressure** (BDF) [50.0 Hz]	51.93147	-177.1275	203	2.9324

KIRH	Velocity Sensor* (BHE, BHN, BHZ) [50.0 Hz]	51.89981	-177.0937	321	5.7117
KIWB	Velocity Sensor* (BHE, BHN, BHZ) [50.0 Hz]	51.853	-177.15094	244	7.8712
*Trillium Compact, 120 s, 754 V/m/s-Centaur, 40 vpp **Chaparral 64-UHP2 infrasound 0.01 V/Pa					

We analyze seismograms from $> M5.5$ teleseismic earthquakes with epicenter-to-station distances of $20\text{--}100^\circ$ that occurred between June 2019 and May 2023 (Figure 3). A total of 776 earthquakes meets these criteria at Gareloi and 711 at Kanaga. Data is downloaded from the EarthScope DMC (last accessed May 2023). We cut the seismograms to 10 s preceding and 90 s after the predicted P-wave arrivals using the AK135 global model (Kennett et al., 1995). The data are then downsampled to 25 samples per second using an anti-alias filter, demeaned, detrended, filtered using a bandpass from 0.07 to 2 Hz, and rotated into the vertical-radial-transverse (ZRT) coordinate system.

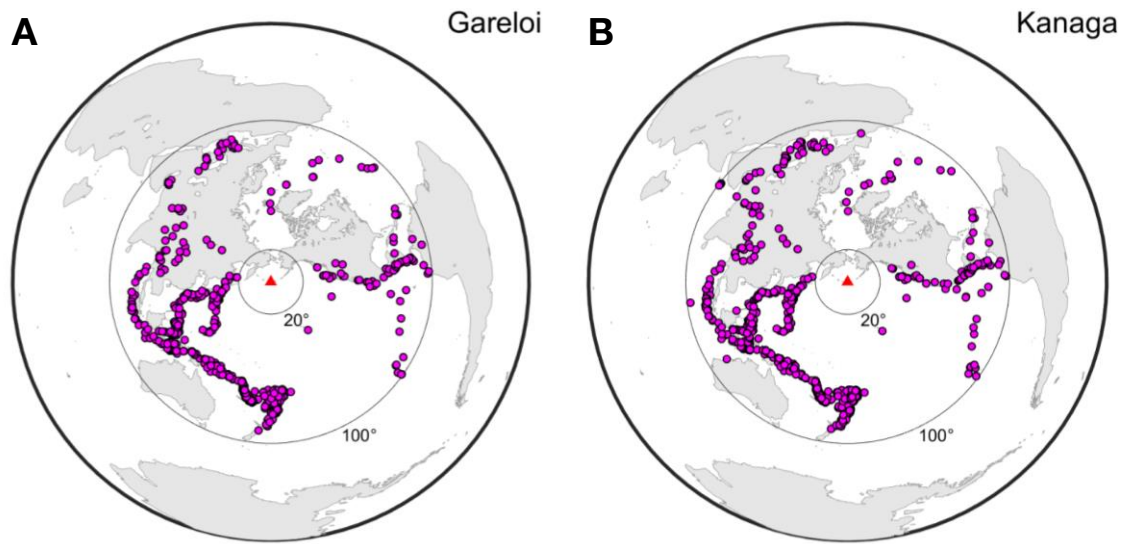


Figure 3: Earthquake event map of teleseismic events 20–100° used for RF analysis. (A) Gareloi used 776 unique earthquake events to produce 5312 RFs across the five stations prior to quality control. (B) Kanaga used 711 unique earthquake events to produce 6789 RFs across the six stations prior to quality control.

2.2 Receiver Function Analysis

We calculate receiver functions (RFs) from the processed teleseismic earthquake seismograms using the time iterative deconvolution method (Ligorria & Ammon, 1999), using a Gaussian width equivalent to a low-pass filter of 0.5 Hz. We employ a series of quality control steps to remove low-quality RFs from our dataset. First, we calculate the signal-to-noise (SNR) ratio of the bandpass filtered seismograms based on comparing 10 s of pre-signal noise to 90 s of signal and discard RFs that have $\text{SNR} < 3$ on the R or Z components. We also discard any RFs that correspond with seismograms that show signs of station malfunctions. Finally, we visually inspect the RFs, and discard those that have significant long-period noise, anomalous reverberations, or negative or low-amplitude first arrivals. After quality control, 2995 total RFs were retained, with a mean of 251 and 290 per station at Gareloi and Kanaga, respectively (see Table 2). Overall, most earthquakes

originate from the west coast of North and Central America, western Pacific subduction zones, central Eurasia, and the mid-Atlantic ridge. This yields back azimuthal coverage that tends to have gaps to the north and southeast at most stations.

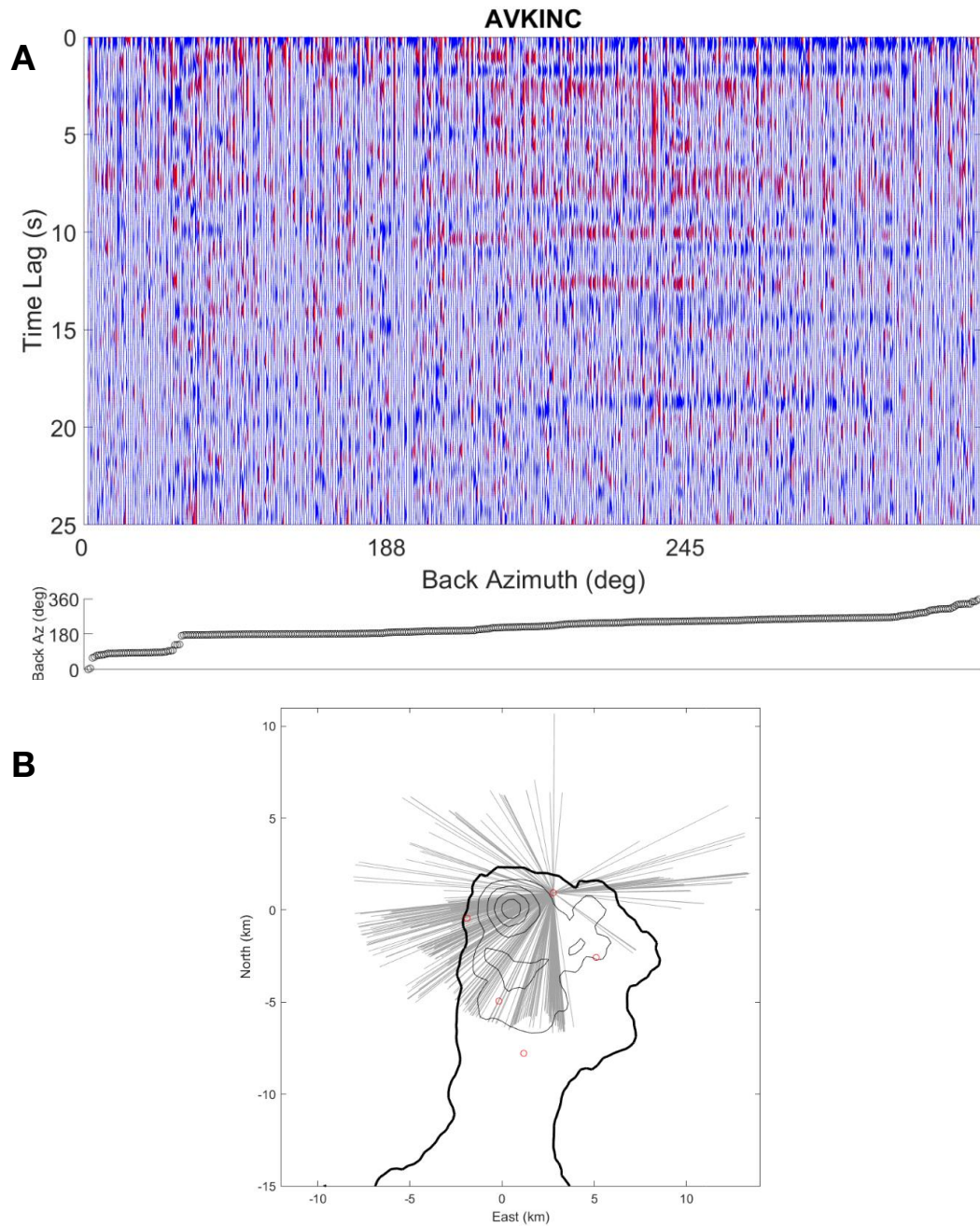


Figure 4: An example station, KINC on the island of Kanaga. (A) A RF stack. (B) The ray path coverage plot for the same station. Both at $\text{SNR} \geq 4$.

Table 2: Number of RFs Used in this Study

Station	Calculated RFs	RFs Used in Data Analysis (After Quality Control + SNR ≥ 3 + bin size ≥ 5)
GAEA	1070	170
GALA	1139	360
GANE	1052	187
GANO	1070	218
GASW	981	321
KICM	1097	263
KIKV	1125	329
KIMD	1135	278
KINC	1176	304
KIRH	1123	241
KIWB	1133	324
Total:	12101	2995

We apply a moveout correction to account for differences in the arrival time of phases in the RFs as a function of the ray parameter, and migrate them to depth. We use a constant velocity model for simplicity, assuming an average crustal $V_p = 6.5$ km/s and $V_s = 3.7$ km/s, broadly consistent with prior velocity constraints along the arc (Shillington et al., 2004; Janiszewski et al., 2013). This allows us to estimate the ray-path coverage of the RFs through the crust. The depth-migrated RFs are stacked into 15° back-azimuth bins to emphasize coherent signals (minimum bin size of 5 RFs). Based on previous observations of RFs in the vicinity of volcanoes (e.g., Janiszewski et al., 2020), we anticipate local changes related to magma storage, which contradicts our 1-D velocity assumption.

However, within an individual 15° back azimuth bin, any deviations from our 1-D velocity assumption should affect data from that bin consistently. Thus, we do not directly interpret the depth of arrivals in terms of structure in this step. Instead, we use the depth migration to consistently stack RFs in a given back azimuthal bin and then analyze the RFs for patterns in their similarity.

Chapter 3: Results

3.1 Directional Variability

We examine the back azimuthal variability of the depth-migrated RFs to provide insight into the crustal structure beneath each volcano using a variety of different approaches. We extract the maximum and minimum RF amplitude between 5 and 40 km depth, as well as its corresponding polarity and depth, for each of the 15° back azimuthally binned RFs at all stations. Furthermore, we convert each back azimuthal bin to “direction toward the volcano” based on the ray path direction and the back azimuth between the individual station and volcanic edifice. A direction of 0° faces towards the volcano, and -180° and 180° faces away, with angles increasing clockwise. We then plot the maximum and minimum RF amplitudes as a function of their corresponding direction relative to the volcano (Figure 5). We visually identify patterns in the depths of the maxima and minima as a function of direction relative to the volcano. At Gareloi, we observe positive maxima followed by negative minima as depth increases from 12 to 26 km between a direction of -80° and 90° that is absent for other directions. Kanaga has a similar pattern between -80° and 80° , with a positive-negative pair observed at depths from 10 to 21 km. We use these visually assessed directions toward the volcano to define directional groupings for the RFs at each station for further analysis.

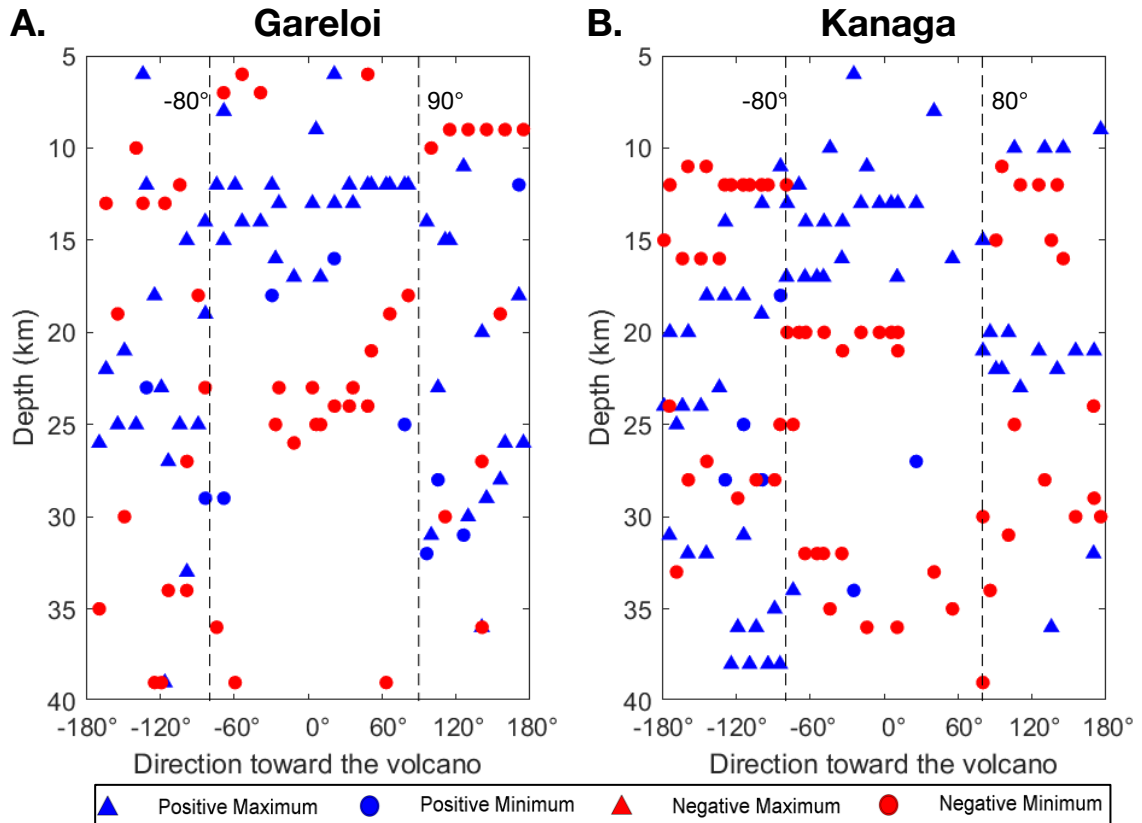
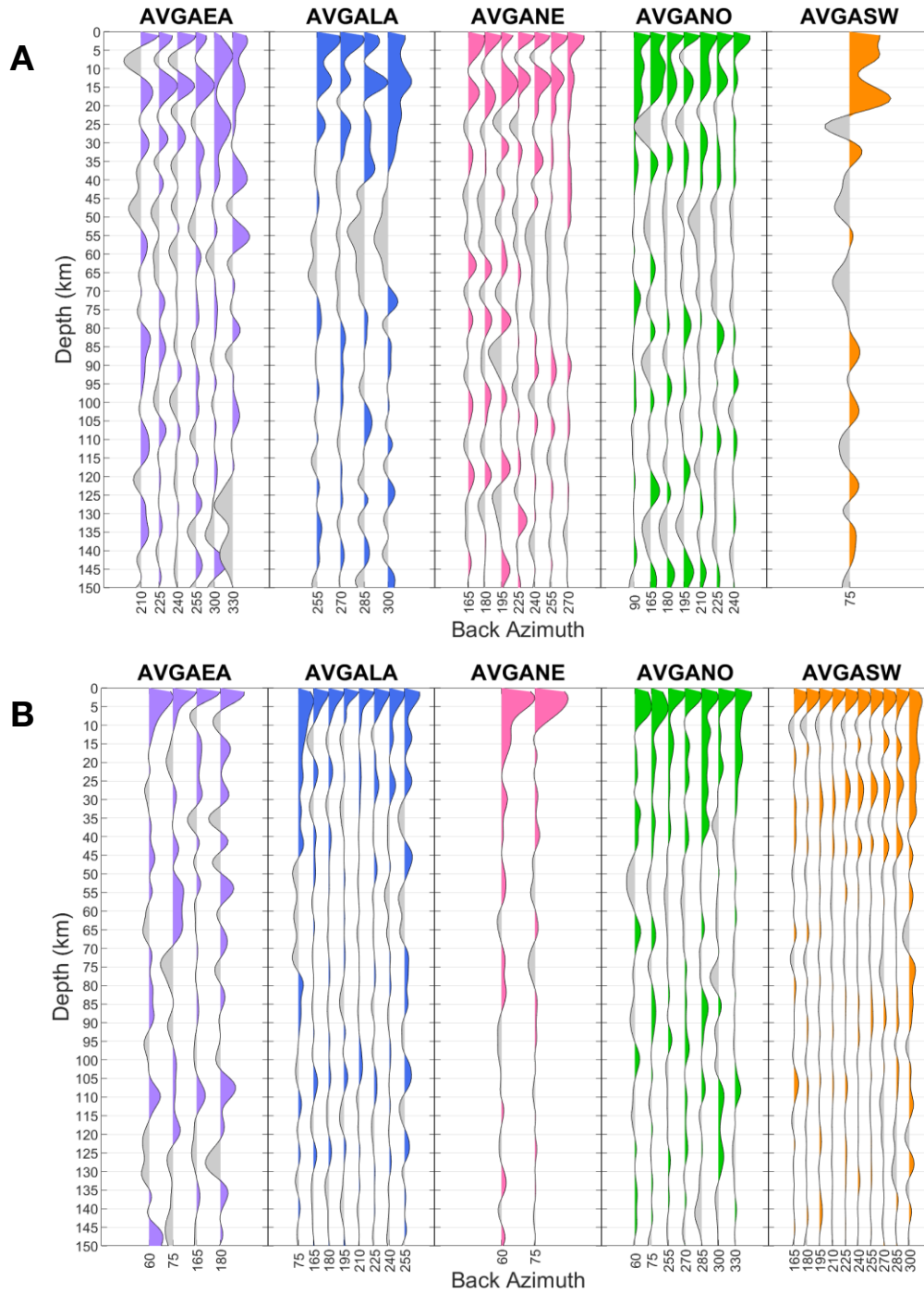


Figure 5: Scatter plots of (A) Gareloi and (B) Kanaga of the maximum and minimum amplitudes of depth migrated 15° binned RFs (at all stations at a volcano) versus depth and organized by direction towards the volcano, with 0° facing towards the volcano and -180° and 180° facing away from the volcano, with angles increasing clockwise. Triangles are maximums, and circles are minimums. Blue represents positive polarity, and red represents negative polarity. Through visual assessment, dashed lines were drawn to highlight patterns of positive maximum and negative minimum at consistent depths: (A) Gareloi with -80° to 90° and (B) Kanaga with -80° to 80° .

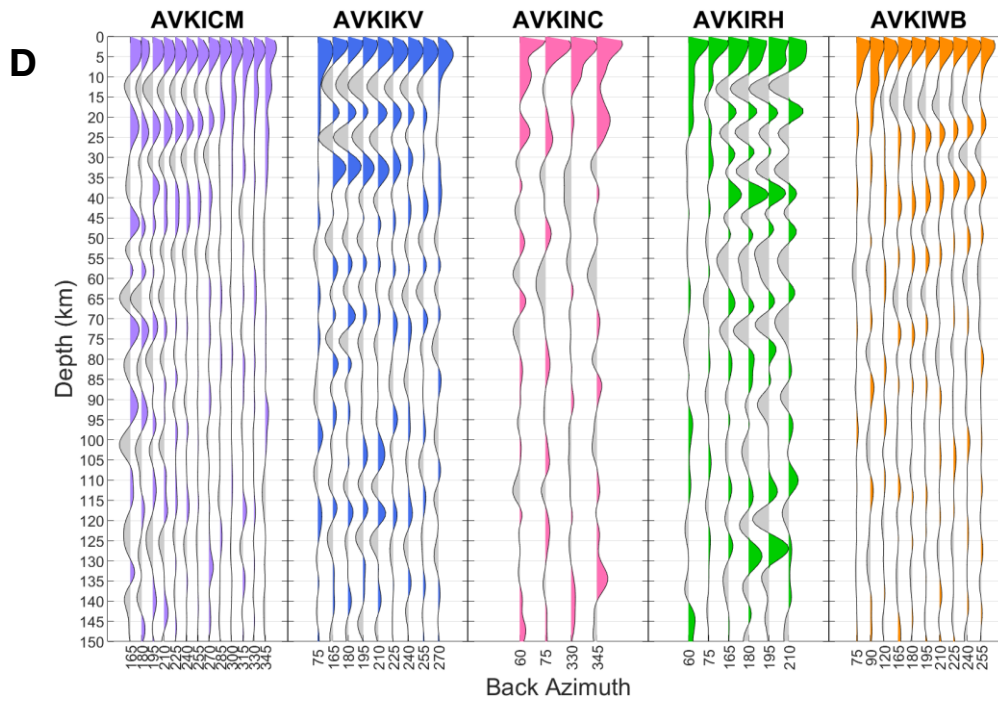
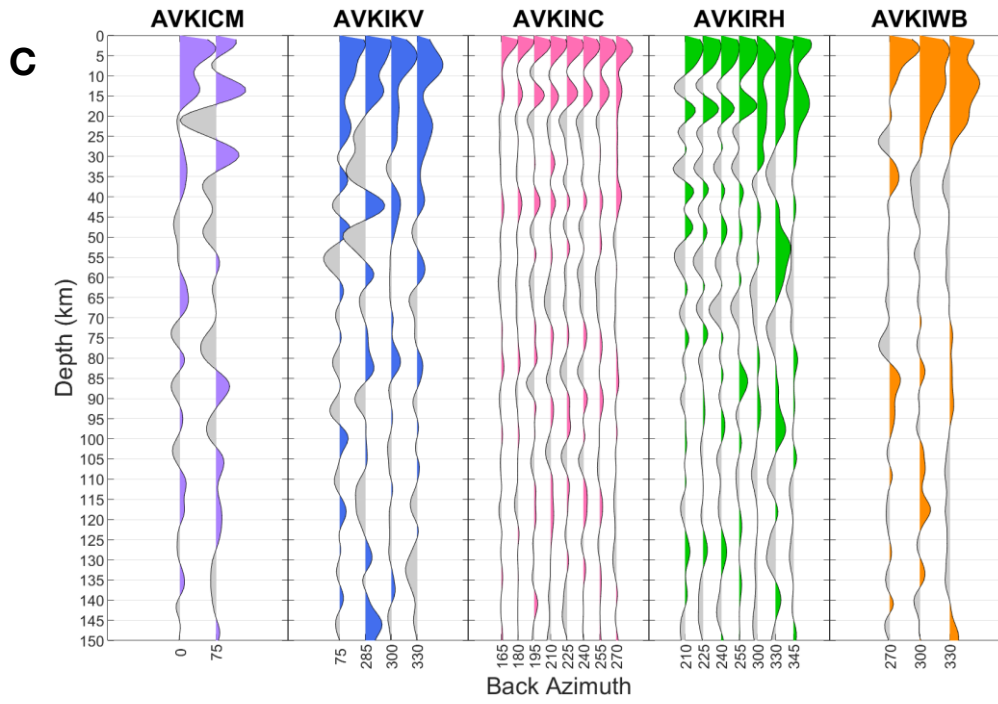
Using the directional cutoffs determined from Figure 5, we plot both the depth-migrated binned RFs pointing towards the volcano and away, and their corresponding ray path coverage plots (Figure 6). For Gareloi, “towards” represents the range -80° to 90° and “away” represents all other angles. In Kanaga’s case, “towards” represents the range -80° to 80° and “away” represents all other angles. Also, station KIMD, being the most southern station on Kanaga is excluded due to a lack of intersecting ray path. Generally, the RFs facing towards the volcano are visually similar to themselves and those facing away are

visually similar to themselves, yet the towards and away RFs are visually dissimilar.

Gareloi



Kanaga



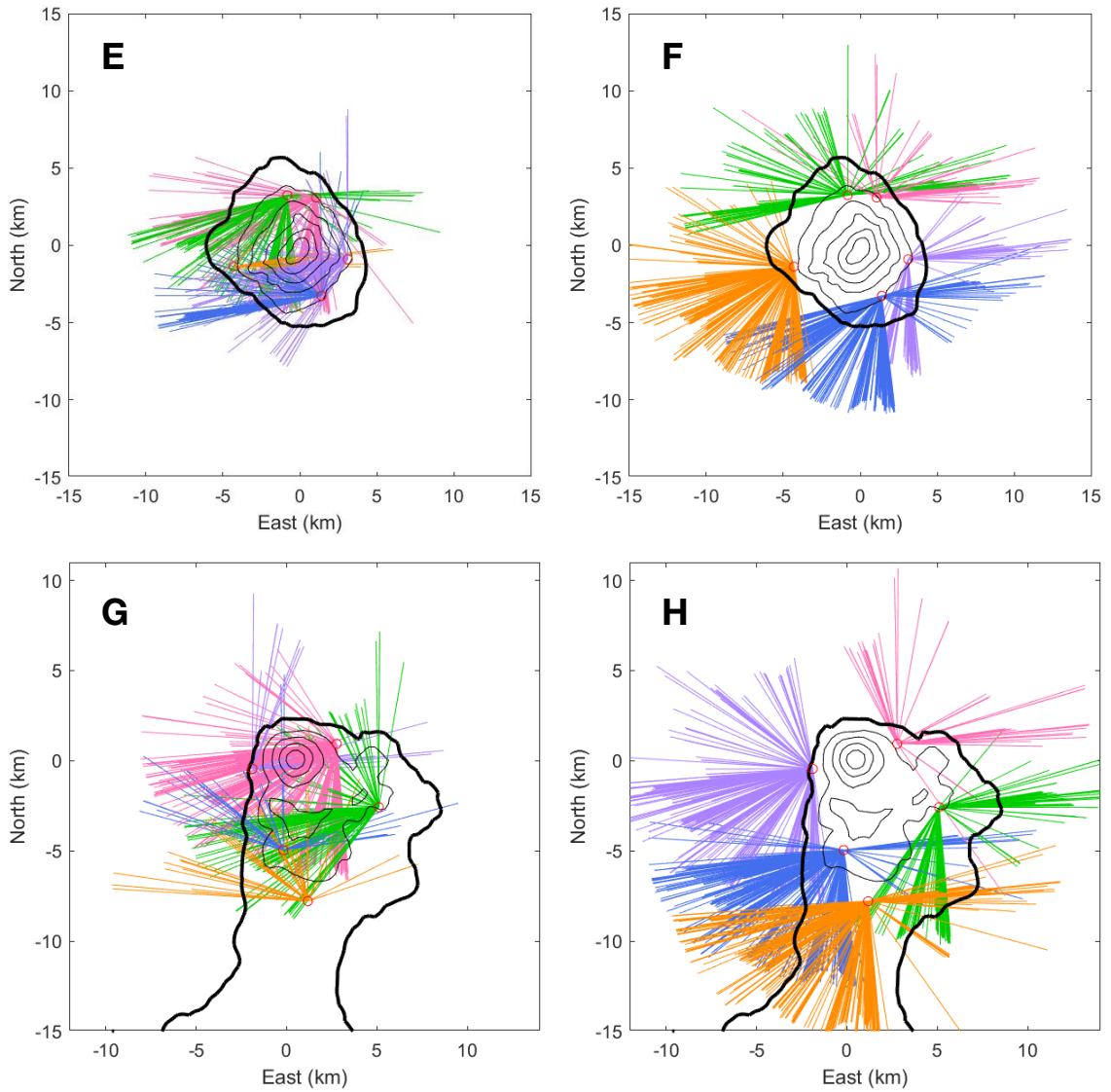
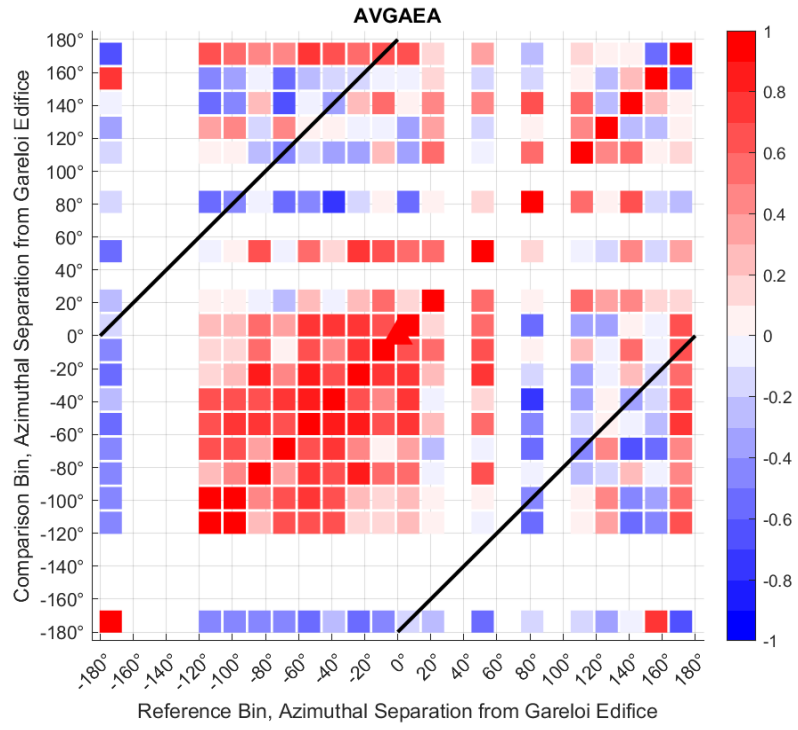
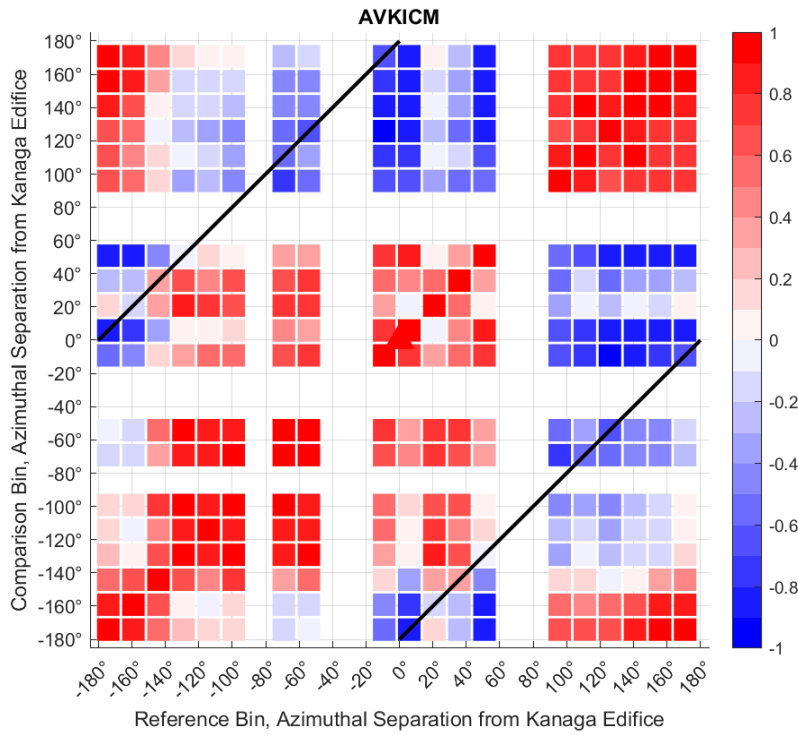


Figure 6: RFs (depth migrated, 15° binned) from all stations (except AVKIMD or station KIMD at Kanaga), whose ray path points towards and away from the volcano edifice were plotted with their corresponding ray path coverage plots. Cutoff angles for toward and away were determined by Figure 5. (A) RFs pointing toward Gareloi and ray path coverage plot (E). (B) RFs pointing away from Gareloi and ray path coverage plot (F). (C) RFs pointing towards Kanaga and ray path coverage plot (G). (D) RFs pointing away from Kanaga and ray path coverage plot.

To further analyze the directional variability of the depth-migrated RFs, we quantify their similarity by calculating the cross-correlation coefficients between all back azimuthally binned RF pairs at a given station (Figure 7). In detail, we choose a reference binned RF and calculate its cross-correlation coefficient with all other binned RFs at a particular station between depths of 5 and 40. We then repeat this, using each back azimuthal bin as a reference RF. We find that there are clear patterns of correlation and/or anticorrelation that vary as a function of back azimuth at most stations.

In all cases, bins that are proximal to each other are highly correlated (denoted along the diagonals in Figure 7). Station GAEA at Gareloi (Figure 7A) shows a high positive correlation at proximal stations that transitions to anticorrelation for ray paths that have back azimuths separated by 180° . Similar features are observed at station KICM at Kanaga (Figure B). Station KIMD on Kanaga (Figure 7C) offers an interesting exception. Here, most RFs are positively correlated, with minimal anticorrelation observed. This suggests that its RFs do not substantially vary as a function of back azimuth, a marked contrast to all other stations, indicating that it is likely imaging more homogenous, simple crustal structures. This station is the farthest from its respective volcanic edifice (~ 18 km), giving a boundary on the potential spatial distribution of crustal magmatic architecture.

A**B**

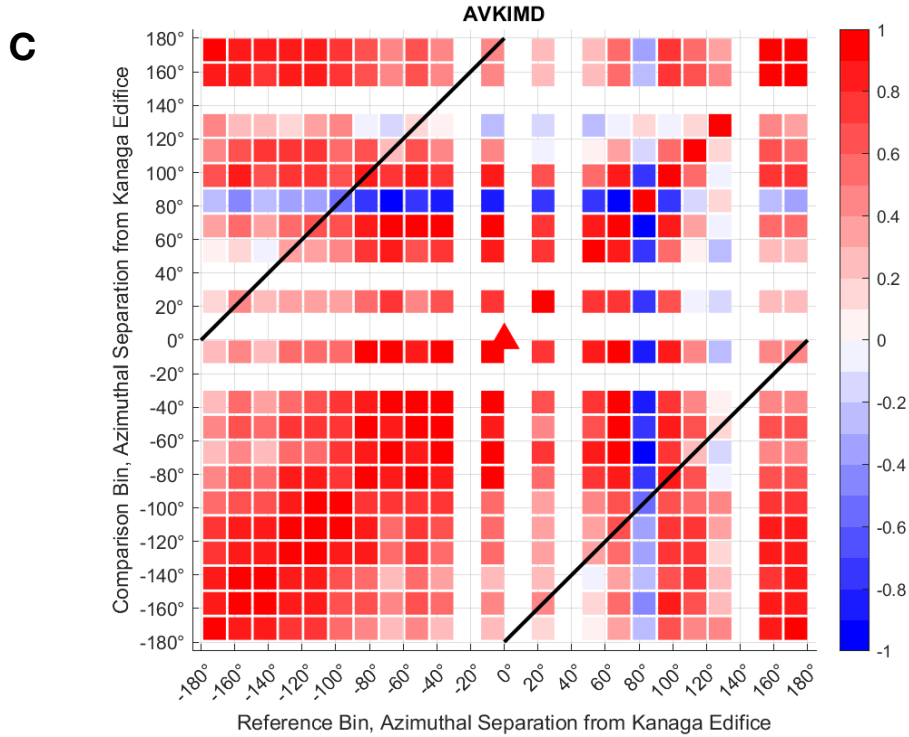


Figure 7: Cross-correlation plot between 15° RF bins with respect to the azimuthal separation or direction from the volcano edifice: 0° is pointing toward the volcano and -180° and 180° are pointing away from the volcano, with angles increasing clockwise. (A) AVGAEA is the station GAEA and is located east-southeast from the Gareloi’s edifice. (B) AVKICM is the station KICM and is located west-southwest of the volcano Kanaga. (C) AVKIMD is the station KIMD, which is located south-southwest of the volcano Kanaga and is the farthest station from the volcano on Kanaga Island. See Appendix B for the cross-correlation plots at all stations for both volcanoes.

3.2 Synthetic Modeling

Finally, we present results from our investigation comparing synthetic RFs to our observed data. This simultaneously helps to constrain the geographic variability in the RFs, while also investigating possible crustal velocity models to explain the data. We produce synthetic RFs for both a 2-layer and 4-layer velocity model, and we compare these synthetics to the back-azimuthally stacked RFs. We calculate the root-mean-square deviation (RMSD) between each back azimuthally binned RF and the synthetic for all models to estimate the misfit to our data. For all models, we held the P-wave and S-wave

velocities constant for each layer (see Figure 8 for specific values). For the 2-layer model, we allow the crustal thickness to vary between 25 and 40 km thick, yielding a total of 16 models. We use the RMSD to select the best-fit crustal thickness at the two volcanoes, finding a value of 29 km at Gareloi and 39 km at Kanaga. We then use these two crustal thicknesses in our 4-layer models. The 4-layer model consists of a crustal layer, a low-velocity zone (LVZ), a crustal layer, and the mantle. The thickness and depth of the LVZ are allowed to vary in 1 km increments, yielding a total of 143 tested models. The 4-layer model that best fits Gareloi has an LVZ located at 2-4 km depth, while the best fit for Kanaga has an LVZ at 4–5 km depth.

It is worth emphasizing that we do not consider this to be a full exploration of the model space; thus, we do not specifically interpret the resultant specific velocity models at this time. Instead, we treat these as potential end-member models and examine the geographic patterns of where different back-azimuthal bins tend to be better fit by either the 2-layer or 4-layer model.

Overall, we observe that back azimuthal bins with ray paths beneath and pointing towards the volcano edifice had a lower RMSD for the 4-layer model than the 2-layer model. In areas where the ray paths point away from the volcano, the 2-layer model had a lower RMSD than the 4-layer model (Figure 9; additional tested models are available in Appendix B). When we only examine the RMSD, we see variability across stations, with some tending to have larger or smaller misfits between the synthetic and RF data. For example, station KIMD at Kanaga has consistently low RMSDs, particularly for the 2-layer model, with little back azimuthal variation. This is consistent with the observations from the cross-correlation analysis, suggesting a relatively simple, isotropic crustal structure

beneath this station. By contrast, other stations at Kanaga, and Gareloi show significant back azimuthal variability in their RMSDs for the 2-layer and 4-layer models. The patterns of back azimuthal variability are better emphasized by examining the difference between the 4-layer and 2-layer model RMSDs.

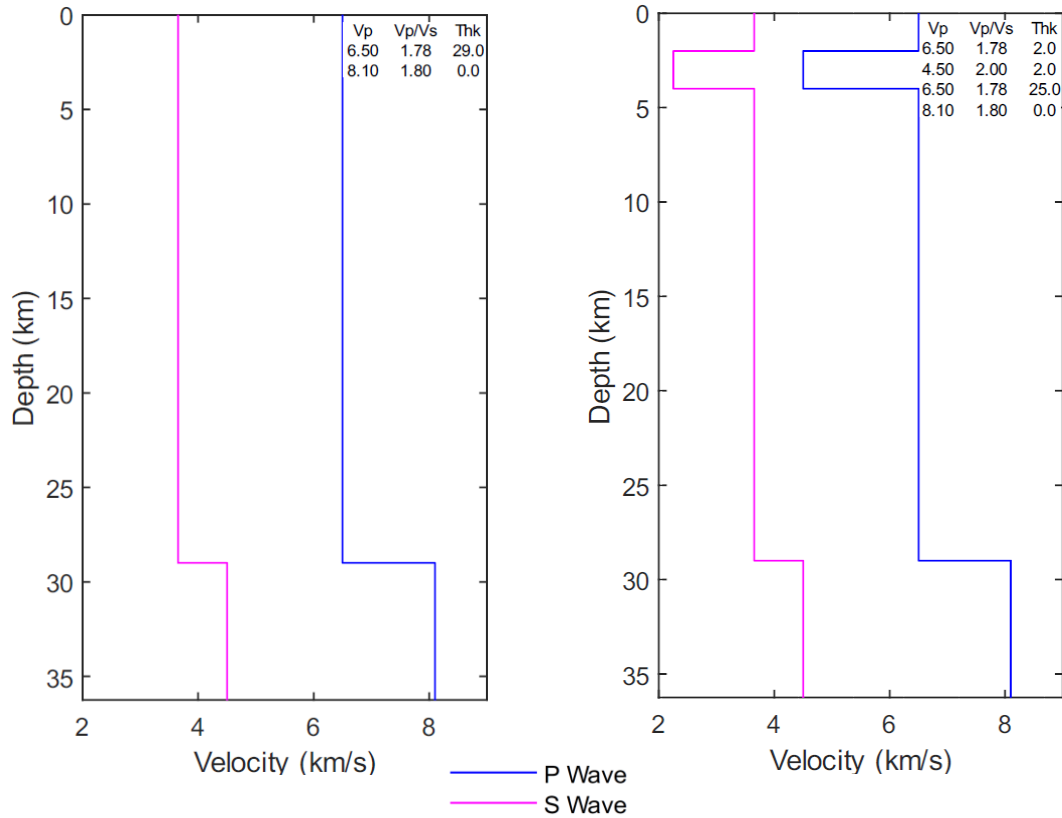
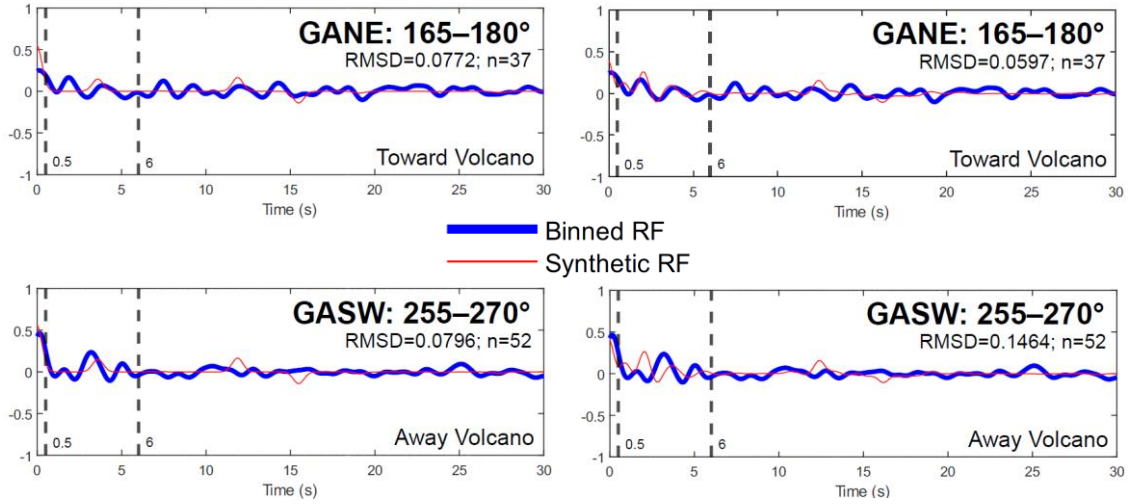
The RMSD differences were calculated by subtracting all 2-layer RMSD at each back azimuthal bin at each station from its corresponding RMSD in the 4-layer model. Figure 10 subtracts the models described in Figure 9. Positive values, colored blue, indicate a better fit for the 2-layer model. Negative values, colored yellow/red, indicate a better fit for the 4-layer model. For Gareloi (Figure 10A), most of the ray paths that point away to the south are a better fit for the 2-layer model, while ray paths that point directly toward the volcano edifice better fit the 4-layer model. The red ray paths pointing toward the volcano edifice appear symmetrical or centered on the volcano. Similarly, the ray paths directly below the volcano edifice of Kanaga (Figure 10B) were negative and a better fit to the 4-layer model, whereas almost all other back azimuthal bins were positive and better fit the 2-layer model. However, the negative values were not centered around Kanaga's edifice, but rather are asymmetric, with part of the south of the edifice and much of the north of the edifice having negative values, better fitting the 4-layer velocity model. While further work is needed to improve the exploration of velocity models, this result indicates a clear data-driven pattern that more complex crustal structure better explains RF observations in the vicinity of the Kanaga and Gareloi volcanoes.

2-layer Model

4-layer Model

A.

Gareloi



B. Kanaga

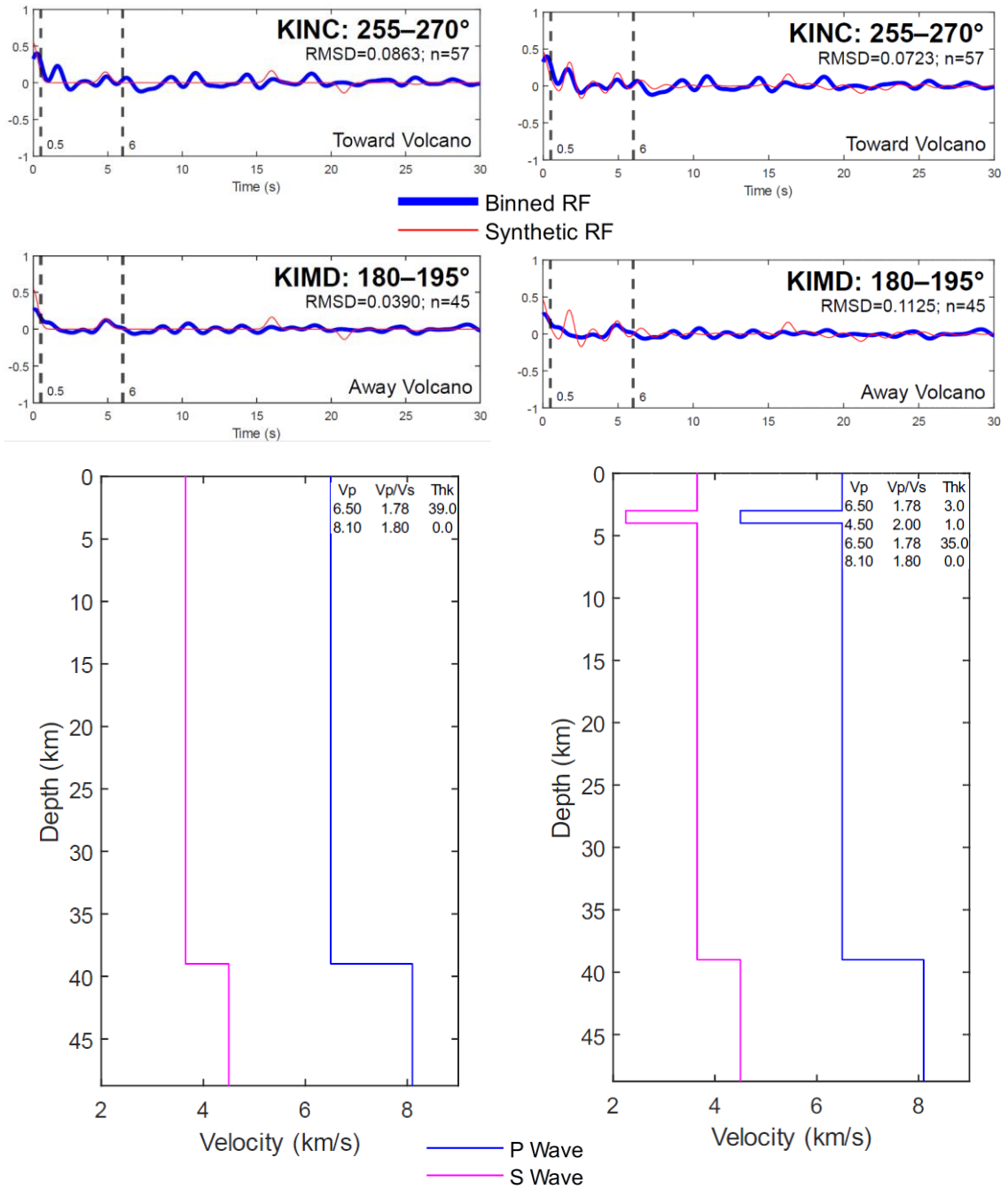


Figure 8: Synthetic RFs plotted against a 15° back azimuthal binned RF pointing towards the volcano edifice and away for both a 2-layer model and a 4-layer model. The corresponding velocity models are plotted. The RMSD between the synthetic and binned RFs is listed, and the number of individual RFs in each bin is listed. (A) Gareloi example stations: GANE (towards) and GASW (away). (B) Kanaga example stations: KINC (towards) and KIMD (away).

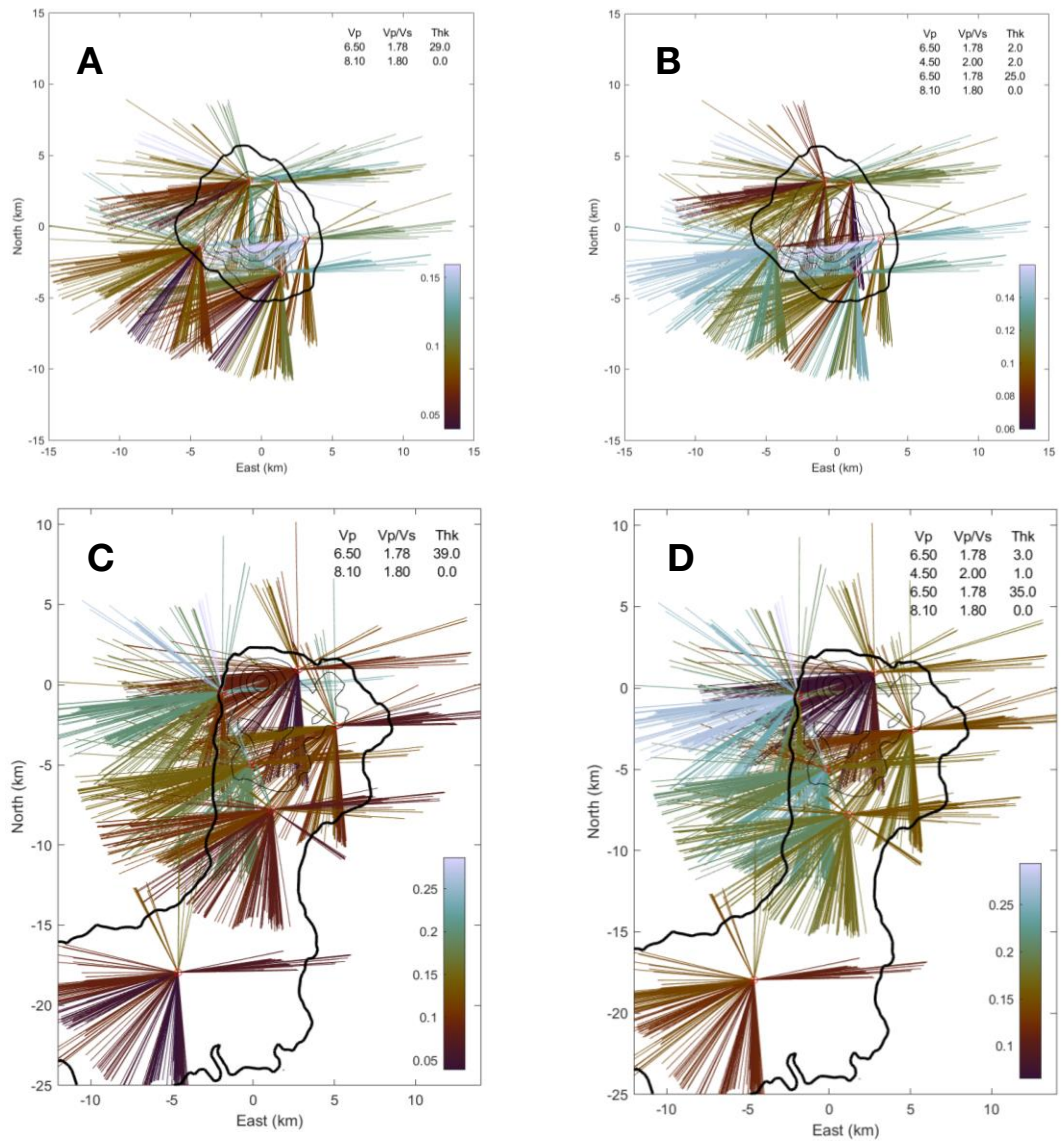


Figure 9: RMSD plots computed from 15° back azimuthal binned RFs and synthetic RFs for both a 2-layer and 4-layer velocity model at Gareloi and Kanaga. Shown here are only the models with the lowest RMSD at all stations for the 2-layer and 4-layer model at each volcano. (A) Gareloi 2-layer velocity model. (B) Gareloi 4-layer velocity model. (C) Kanaga 2-layer velocity model. (D) Kanaga 4-layer velocity model.

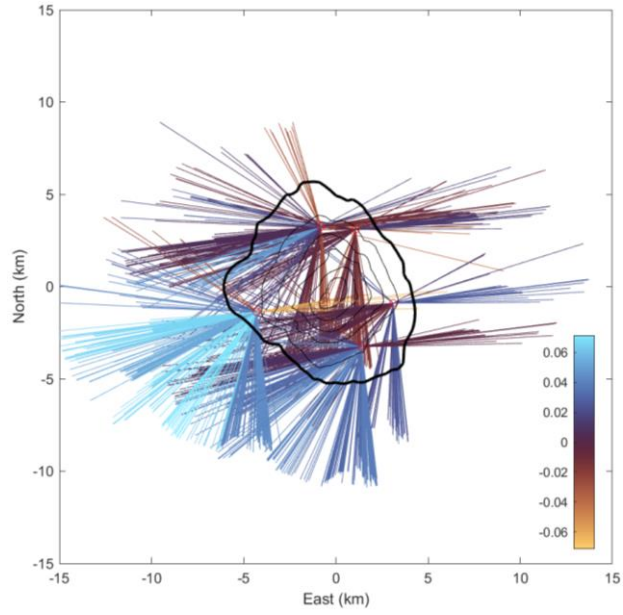
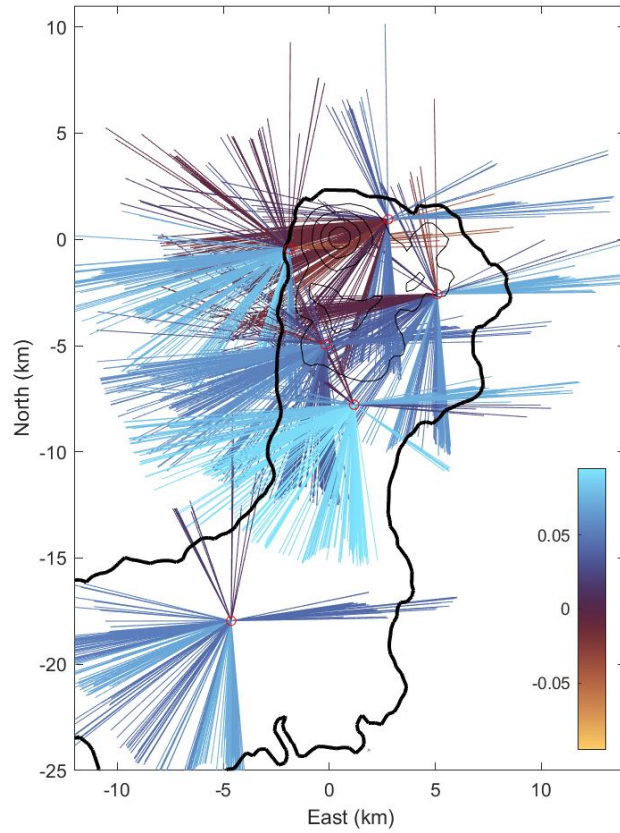
A**B**

Figure 10: RMSD difference plots for (A) Gareloi and (B) Kanaga. The RMSD difference is calculated by subtracting the 2-layer model RMSD from the 4-layer model RMSD. The models in Figure 9 were used to produce these two plots. Positive values (blue) imply a better fit to the 2-layer model. Negative values (yellow/red) imply a better fit to the 4-layer model.

Chapter 4: Discussion

The back azimuthal variability in the RFs at each volcano is complex; however, some patterns exist. Examining Figures 5 and 6 indicates that the RFs toward and away from the volcano are generally different in terms of waveform, such as when certain peaks occur and the strength of the signal. Figure 7 and Appendix A quantify these similarities and differences between RFs at each station. For example, stations KICM and KINC of Kanaga, both have a range of directions relative to the volcano edifice, where the RFs that point toward the volcano edifice have a high positive correlation and those pointing away have no correlation or are anticorrelated. One possibility is that the structure directly beneath the volcano edifice is vastly different from the structure beneath the edges of the volcano and off to the sides. We speculate that the existence of a LVZ beneath the volcano edifice represents persistent magma storage. The plausibility of a crustal LVZ beneath the volcano edifice is not unreasonable, especially since both volcanoes are relatively active and Kanaga experienced the most recent eruption in 2023 (Global Volcanism Program, 2023). The RMSD difference plots (Figure 10) support a case where the 4-layer model best fits beneath the volcano edifice and the 2-layer model best fits the surrounding region. These plots indicate that Gareloi has a nearly symmetric geographical LVZ centered at the volcano edifice, while Kanaga appears to be asymmetrical and extends further north and a bit southward from the edifice.

Note that although these patterns exist in the RMSD difference plots (Figure 10), we were only able to compare two models that had the lowest RMSD along all stations at the volcano. Each station's best-fit model may not be identical to another station's best-fit

model. Each back azimuthal bin could also be best fitted to different models. We were unable to formally and robustly search the model space to find a model that fits best. The analysis done in Figure 10 shows that it is plausible for a LVZ to explain the variability in the receiver functions. In addition, certain back azimuthal bins show consistently low or high RMSD (Figure 9), which adds a level of complexity when making decisions on which model is a better fit.

Station KIMD on Kanaga Island is the farthest removed from the volcano edifice. It is presumed that the structure beneath the station is relatively simple in comparison to the stations near the volcano edifice. The cross-correlation plot of station KIMD (Figure 7C) is almost all positively correlated everywhere, indicating a relatively uniform structure beneath the volcano. In all 16 2-layer velocity models, station KIMD always had a relatively low RMSD for all back azimuths. This is supported by Figure 10 which shows it is a better fit for the 2-layer model. It is reasonable to assume that station KIMD exists on a relatively simple crustal layer.

Chapter 5: Conclusion

In this study, we examine crustal magmatic storage at two active volcanoes along the Aleutian arc, Gareloi and Kanaga. We use a seismic imaging technique called RFs, which are sensitive to abrupt boundary changes, to constrain the depth and velocity of magma chambers beneath the volcanoes.

To explore the complex subsurface structure at both volcanoes, RFs were compared toward and away. By visual inspection, cutoff directions toward the volcanoes were determined to be -80° to 90° at Gareloi and -80° to 80° at Kanaga. The RFs pointing towards the volcano were similar in waveform, and the RFs pointing away from the volcano were also similar in waveform; however, the RFs pointing toward and away from the volcano edifice were noticeably different. To further examine the similarities and differences, cross-correlation plots were produced from depth-migrated RFs for the upper 5–40 km, which indicate that some stations clearly show a high degree of similarity or correlation for a direction toward the volcano, then abruptly show no correlation or anticorrelation at other directions. There appears to be a pattern of similar RFs pointing toward the volcano.

We hypothesize the existence of a persistent crustal magmatic chamber under each volcano, which would be represented as a LVZ. The RFs pointing toward the volcano edifice are likely represented by a LVZ, while RFs pointing away from the volcano edifice are likely described by a simple crustal model. Synthetic RFs were used to compare a 16 2-layer model (crust and mantle) and 143 4-layer model (crustal LVZ model). The root-mean-square deviation (RMSD) was computed for each model at each back azimuthal bin,

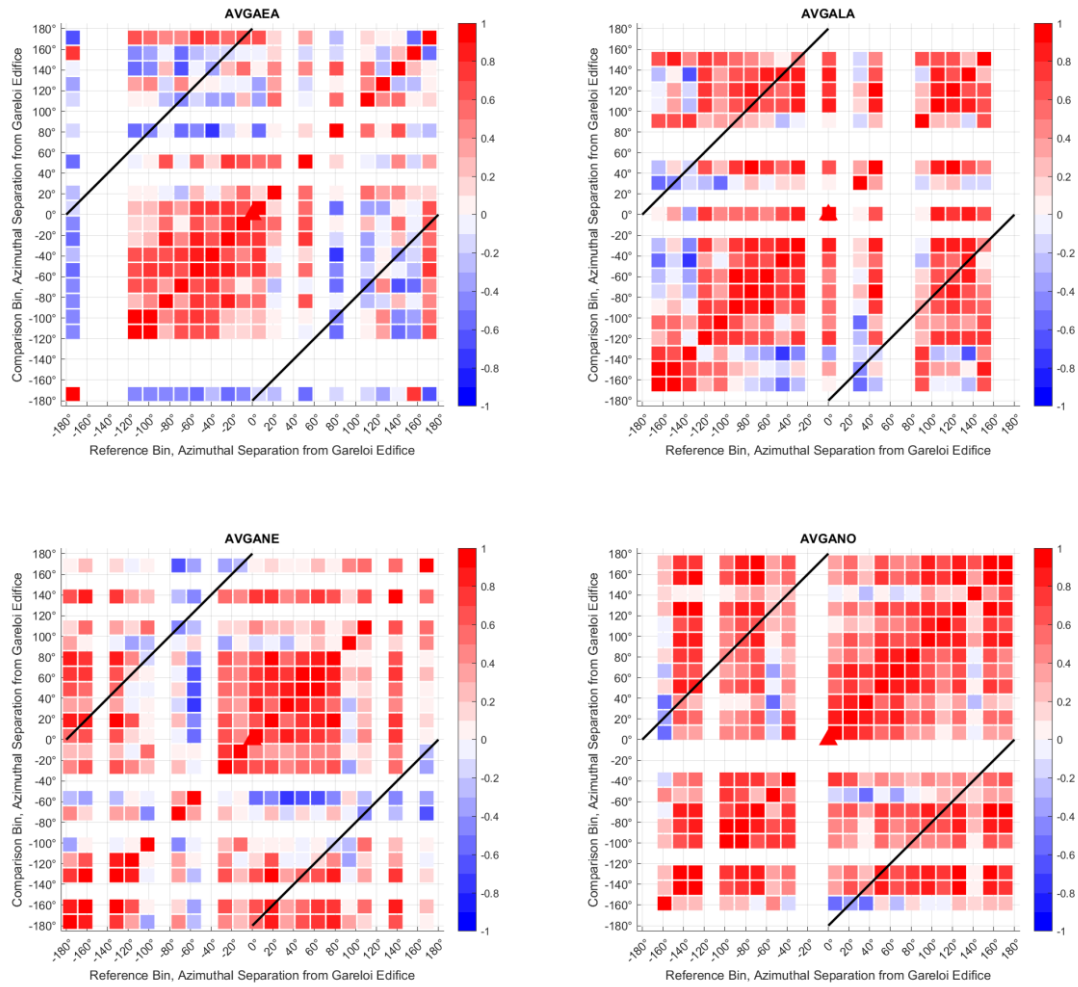
and the best models were chosen. Finally, a plot was produced by subtracting the RMSD values for the 2-layer from the 4-layer model. The 2-layer model best fits the ray paths pointing away from each volcano's edifice, and the 4-layer model best fits the ray paths pointing toward and beneath each volcano's edifice.

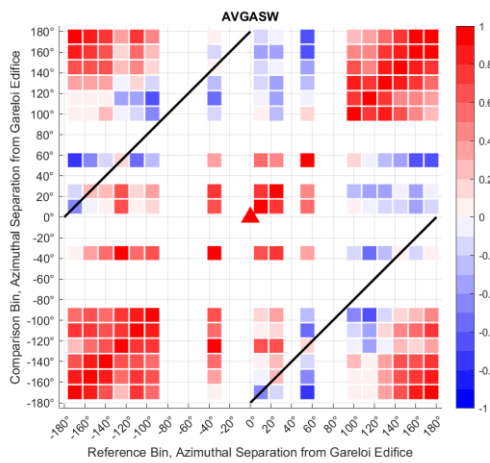
Although this is not a comprehensive study of the model space, it implies that some of the variability could be explained using a LVZ. More work is needed to be able to constrain magma depth at the two volcanoes, Gareloi and Kanaga.

Appendix A: Cross-Correlation Plots

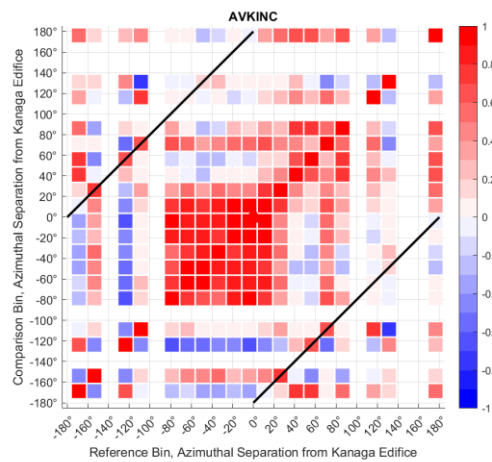
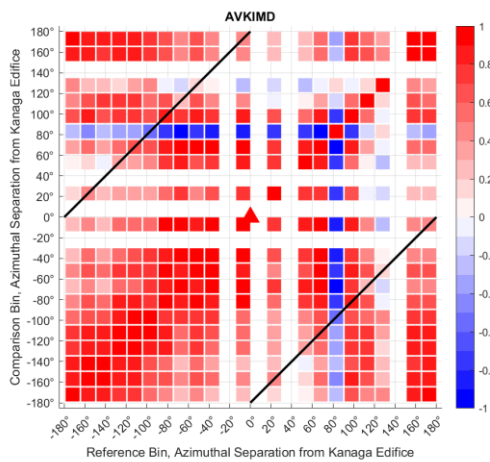
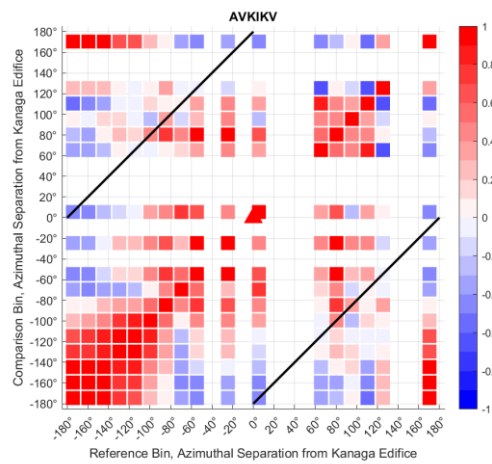
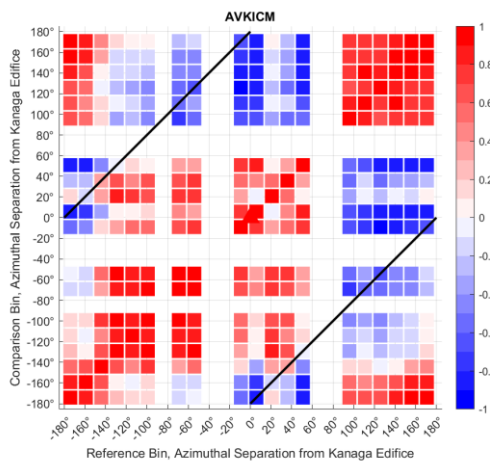
Here are all the cross-correlation plots from all 11 stations and organized by volcano.

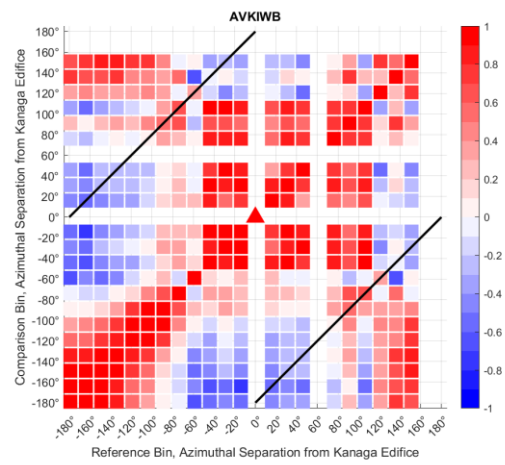
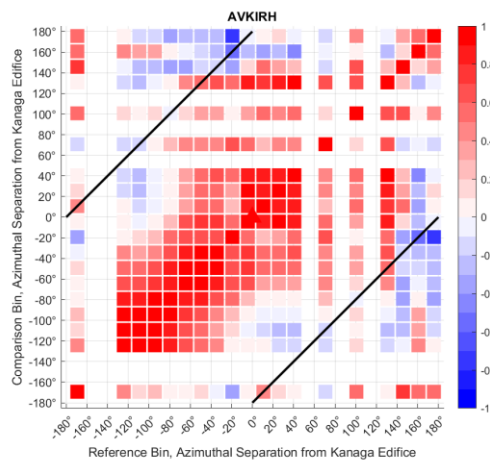
Garleoi





Kanaga

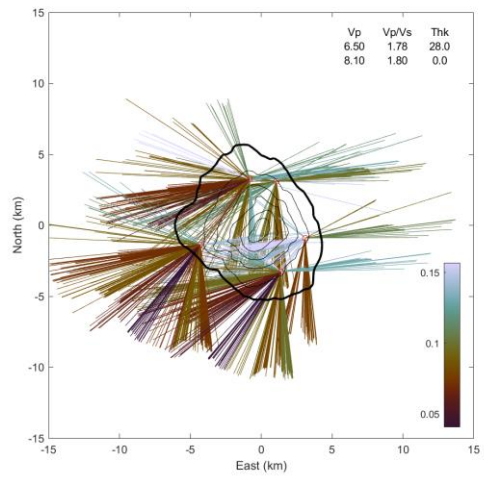
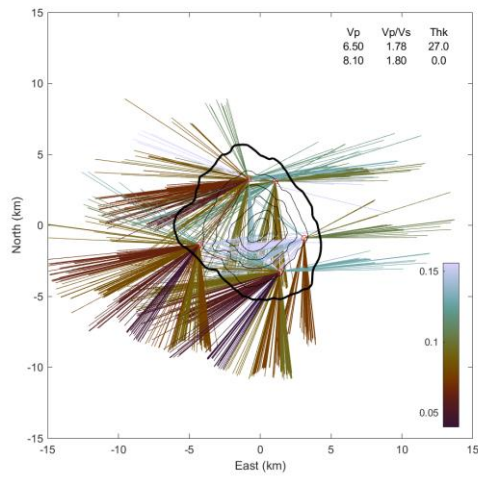
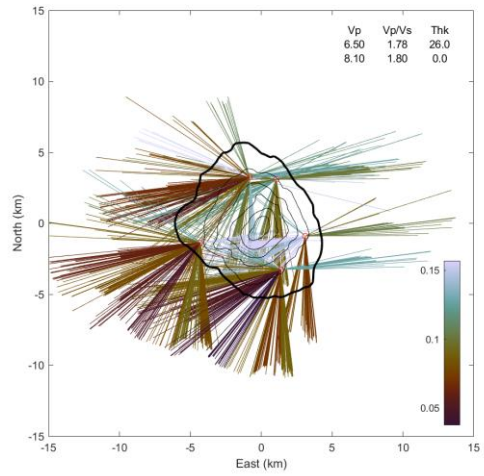
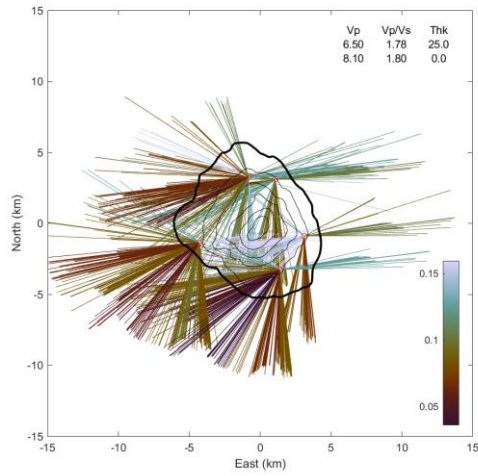


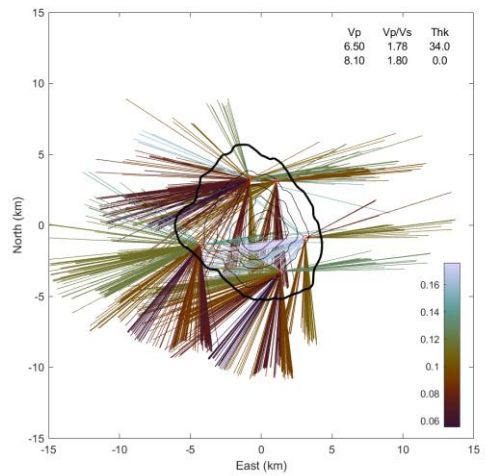
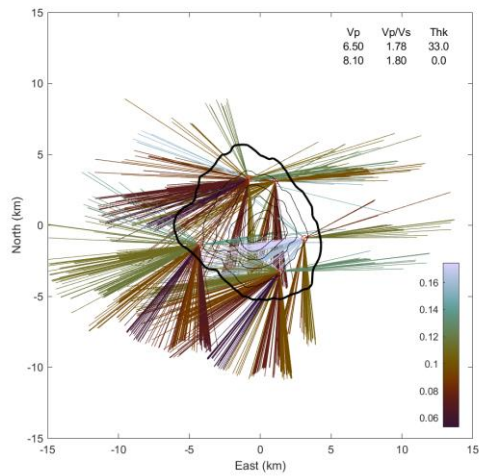
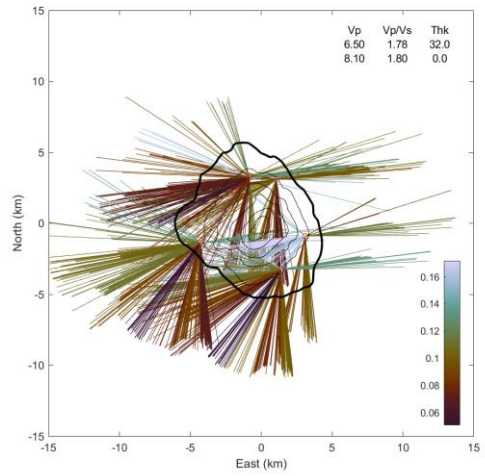
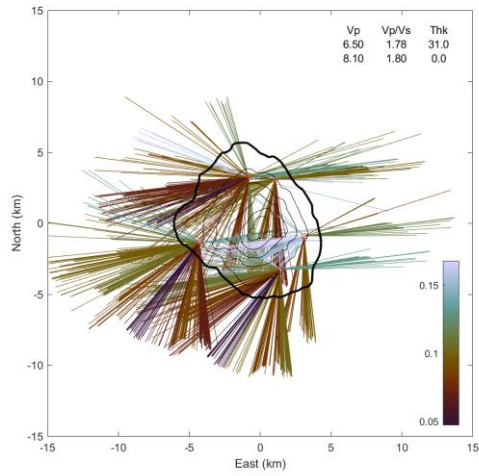
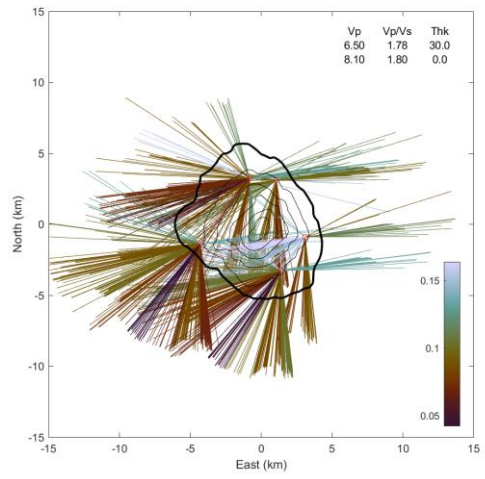
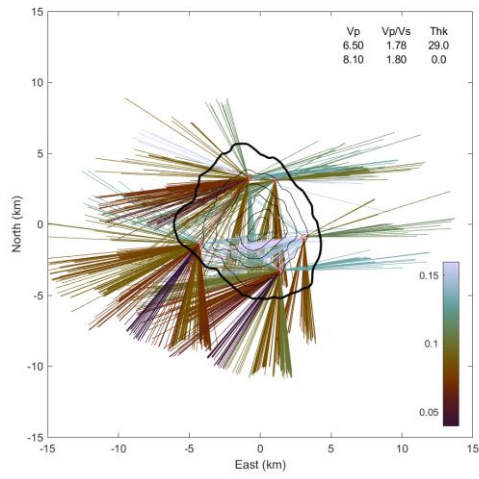


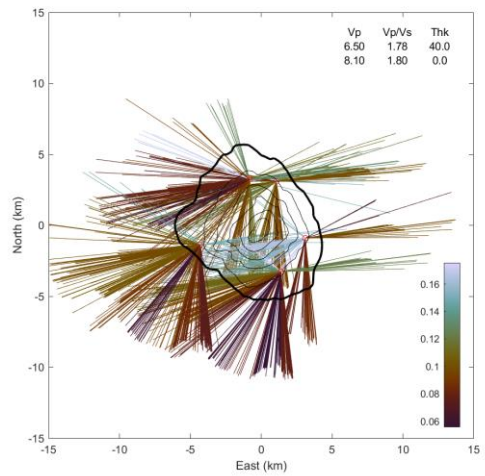
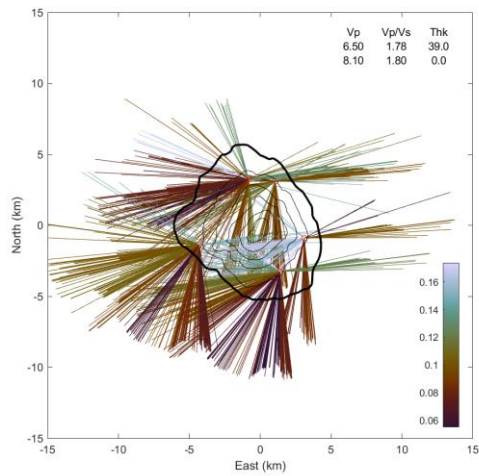
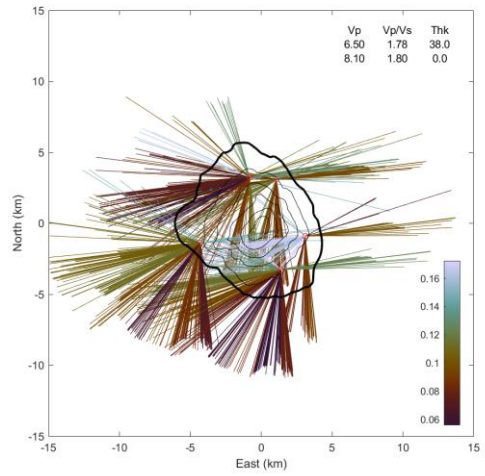
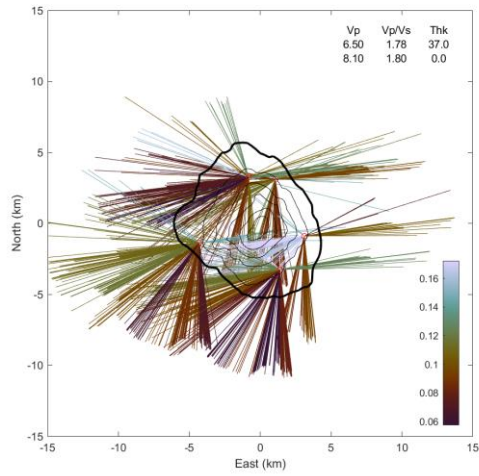
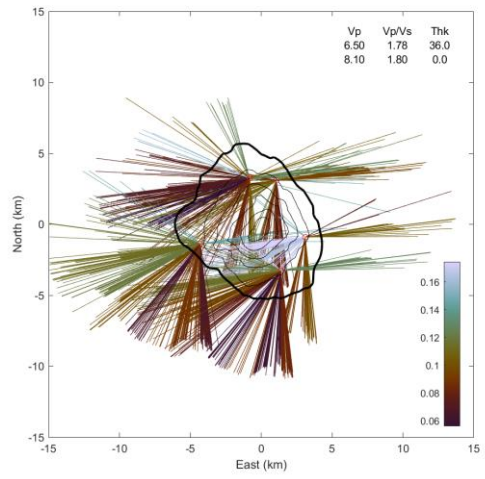
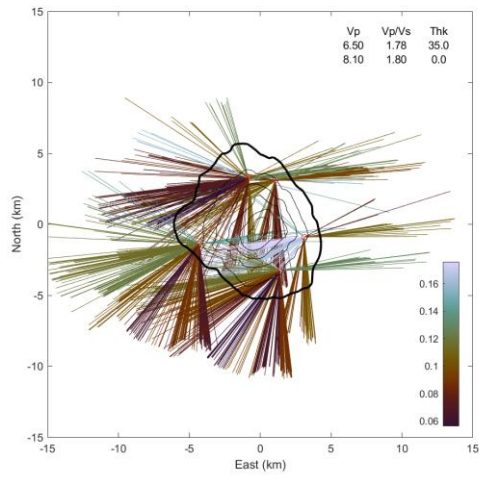
Appendix B: 2-layer RMSD Plots

Here are all the 2-layer RMSD plots for Gareloi and Kanaga.

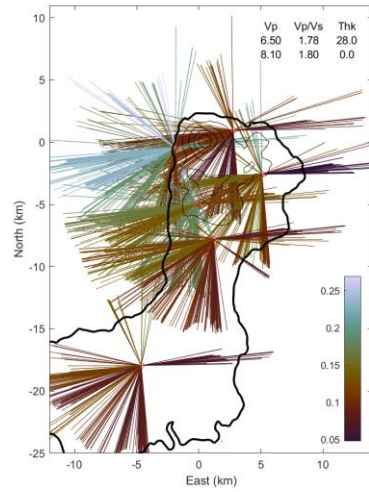
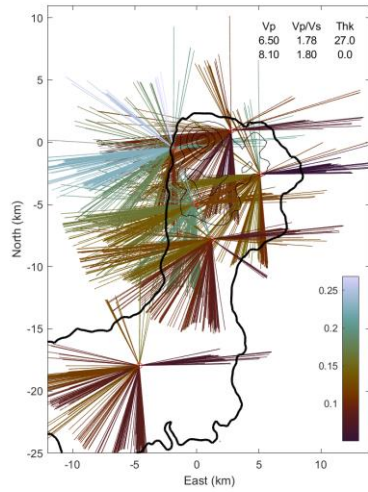
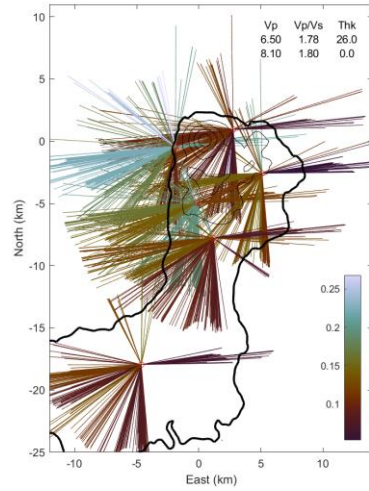
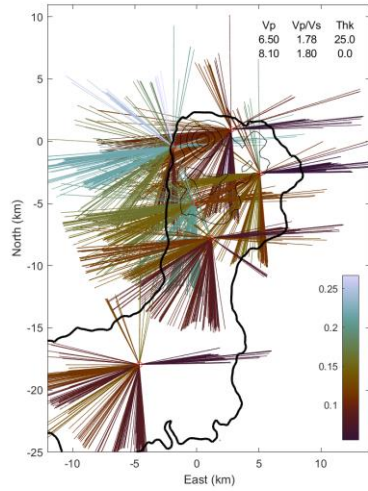
Gareloi

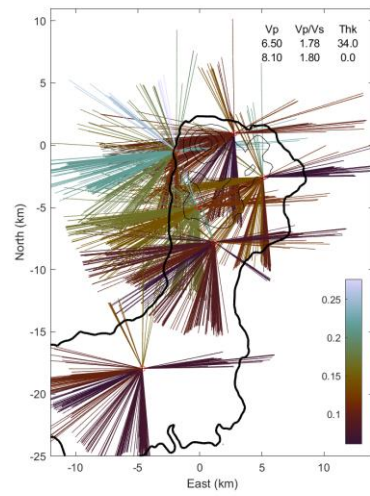
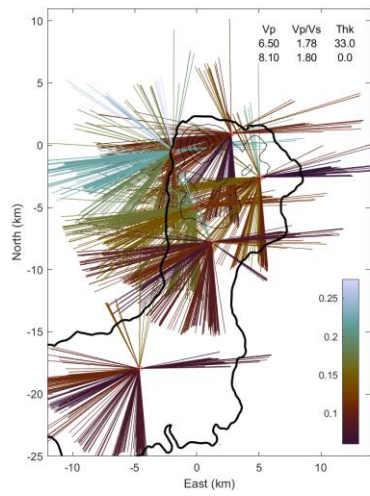
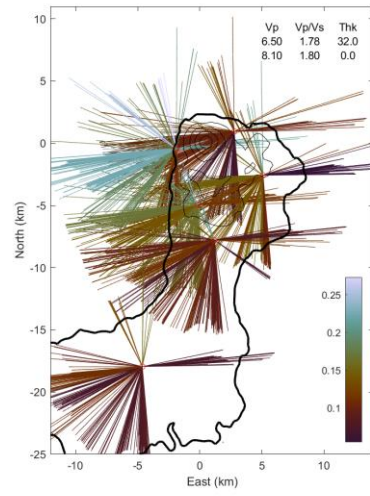
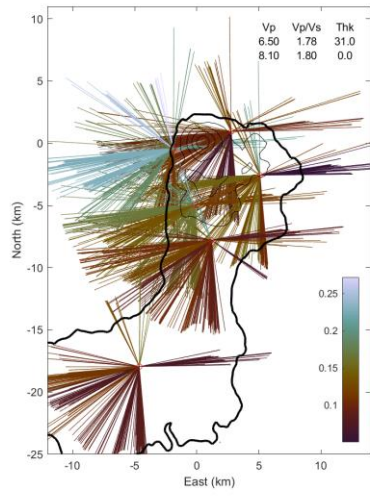
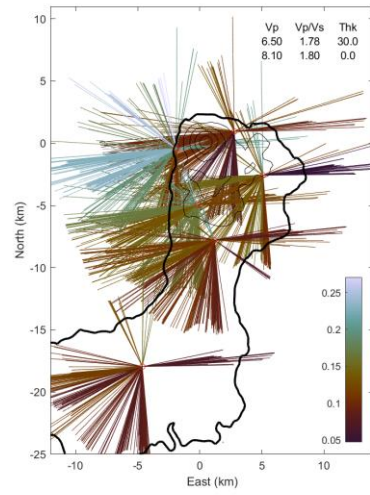
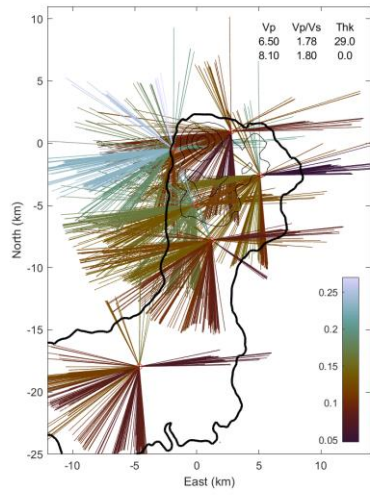


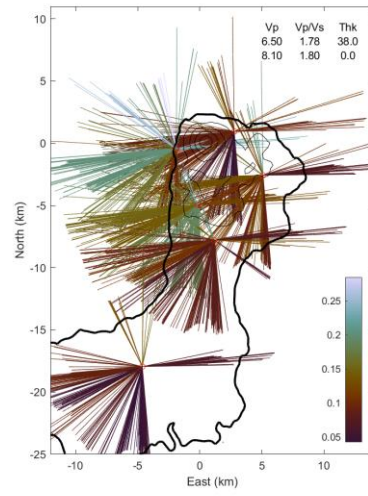
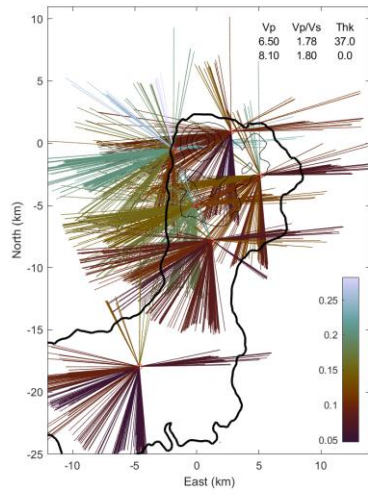
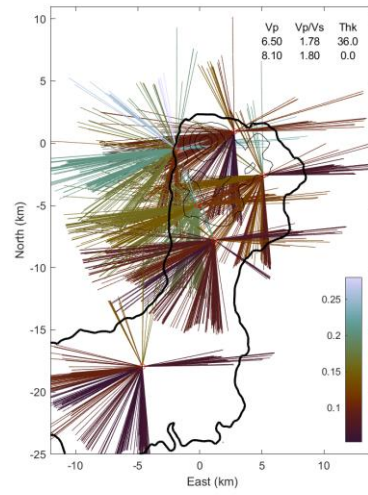
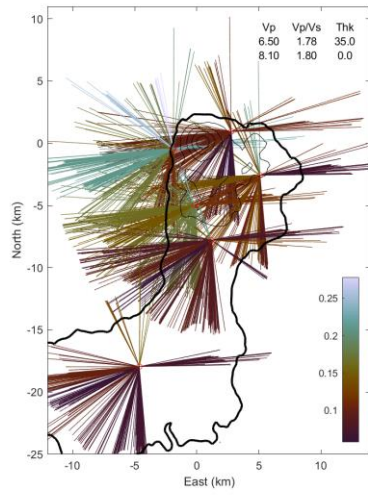




Kanaga







References

- Buurman, H., Nye, C. J., West, M. E., & Cameron, C. (2014). Regional controls on volcano seismicity along the Aleutian arc. *Geochemistry, Geophysics, Geosystems*, 15, 1147–1163. <https://doi.org/10.1002/2013GC005101>
- Coombs, M. L., White, S. M., & Scholl, D. W. (2007). Massive edifice failure at Aleutian arc volcanoes. *Earth and Planetary Science Letters*, 256, 403–418. <https://doi.org/10.1016/j.epsl.2007.01.030>
- DeMets, C., Gordan, R. G., & Argus, D. F. (2010). Geologically current plate motions. *Geophysical Journal International*, 181, 1–80. <https://doi.org/10.1111/j.1365-246X.2009.04491.x>
- Dixon, J. P., Stihler, S. D., Haney, M. M., Lyons, J. J., Ketner, D. M., Mulliken, K. M., et al. (2019). Catalog of Earthquake Parameters and Description of Seismograph and Infrasound Stations at Alaskan Volcanoes—January 1, 2013, through December 31, 2017. *Data Series* (Data Series 1115). Anchorage, AK: U.S. Geological Survey. <https://doi.org/10.3133/ds1115>
- Geist, E. L., Childs, J. R., & Scholl, D. W. (1988). The origin of summit basins of the Aleutian Ridge: Implications for block rotation of an arc massif. *Tectonics*, 7(2), 327–341. <https://doi.org/10.1029/TC007i002p00327>
- Global Volcanism Program, (2023). Report on Kanaga (United States) (Sennert, S, ed.). Weekly Volcanic Activity Report (20 December-26 December 2023). Smithsonian Institution and US Geological Survey.
- Janiszewski, H. A., Abers, G. A., Shillington, D. J., & Calkins, J. A. (2013). Crustal structure along the Aleutian island arc: New insights from receiver functions constrained by active-source data. *Geochemistry, Geophysics, Geosystems*, 14(8), 2977–2992. <https://doi.org/10.1002/ggge.20211>
- Kennett, B. L. N., Engdahl, E. R., & Buland, R. (1995). Constraints on seismic velocities in the Earth from travel times. *Geophysical Journal International*, 122, 108–124. <https://doi.org/10.1111/j.1365-246X.1995.tb03540.x>
- Larsen, J. F. (2016). Unraveling the diversity in arc volcanic eruption styles: Examples from the Aleutian volcanic arc, Alaska. *Journal of Volcanology and Geothermal Research*, 327, 643–668. <https://doi.org/10.1002/2013GC005101>
- Ligorria, J. & Ammon, C. (1999). Iterative deconvolution and receiver function estimation. *Bulletin of Seismological Society of America*, 89, 1395–1400. <https://doi.org/10.1785/BSSA0890051395>
- Maus, S., Barckhausen, U., Berkenbosch, H., Bournas, N., Brozena, J., Childers, V., et al. (2009). EMAG2: A 2–arc min resolution Earth Magnetic Anomaly Grid compiled from satellite, airborne, and marine magnetic measurements. *Geochemistry, Geophysics, Geosystems*, 10, Q08005. <https://doi.org/10.1029/2009GC002471>

- Miller, T. P., McGimsey, R. G., Richter, D. H., Riehle, J. R., Nye, C. J., Yount, M. E., & Dumoulin, J. A. (1998). Catalog of the historically active volcanoes of Alaska. *Open-File Report* (Rep. 98-0582). AK: U.S. Geological Survey. <https://doi.org/10.3133/ofr98582>
- Ryan, H. F., Draut, A. E., & Scholl, D. W. (2012). Influence of the Amlia fracture zone on the evolution of the Aleutian Terrace forearc basin, central Aleutian subduction zone. *Geosphere*, 8(6), 1254–1273. <https://doi.org/10.1130/GES00815.1>
- Shillington, D. J., Van Avendonk, H. J. A., Holbrook, W. S., Kelemen, P. B., & Hornbach, M. J. (2004). Composition and structure of the central Aleutian island arc from arc-parallel wide-angle seismic data. *Geochemistry, Geophysics, Geosystems*, 5(10), Q10006. <https://doi.org/10.1029/2004GC000715>
- Singer, B. S., Jicha, B. R., Leeman, W. P., Rogers, N. W., Thirlwall, M. F., Ryan, J., Nicolaysen, K. E. (2007). Along-strike trace element and isotopic variation in Aleutian Island arc basalt: Subduction melts sediments and dehydrates serpentine. *Journal of Geophysical Research: Solid Earth*, 112, B06206. <https://doi.org/10.1029/2006JB00489>